Study of a complex fluid-structure dam-breaking benchmark problem using a multi-phase SPH method with APR

P.N. Sun, David Le Touzé, A.-M. Zhang

Version of Record: https://www.sciencedirect.com/science/article/pii/S0955799719300943
Manuscript_db17fed919088c7d8e038274fc0ffb5e

Study of a complex fluid-structure dam-breaking benchmark problem using a multi-phase SPH method with APR

P. N. Sun [a], D. Le Touzé [a,*], A.-M. Zhang [b],

[a] *Ecole Centrale Nantes, LHEEA res. dept. (ECN and CNRS), Nantes, France*
[b] *College of Shipbuilding Engineering, Harbin Engineering University, Harbin, China*

Abstract

The present work is dedicated to an accurate modeling of violent Fluid-Structure-Interaction (FSI) problems using a coupled Lagrangian particle method combining a multi-phase δ-SPH scheme and a Total-Lagrangian-Particle (TLP) method. Advanced numerical techniques, *e.g.* Adaptive-Particle-Refinement (APR), have been included in the particle method for improving the local accuracy and the overall numerical efficiency. On one hand, this paper aims to demonstrate the capability of the proposed numerical method in modeling FSI flows with large density-ratios, strong fluid impacts, complex interfacial evolutions and considerable wall-boundary movements and deformations; On the other hand, the numerical results presented in this paper show the importance of considering the existence of air-phase in some complex FSI problems. The entrapped air-bubble, after the free-surface rolling and closing, plays an important role in the overall flow evolution and hence the hydrodynamic load on the structure. Although a density ratio as large as 1000 has been adopted, clear and sharp multi-phase interfaces, which undergo violent breakups and reconnections, are present in the numerical results, and more importantly, stable and smooth pressure fields are obtained. This contributes to an accurate prediction of the structural response, as validated by both the experimental data and other numerical results.

Key words: Smoothed particle hydrodynamics; multi-phase δ-SPH; fluid-structure interaction; multi-particle resolution; large density ratio;

* Corresponding author.
Email addresses: sun.pengnan@ec-nantes.fr (P. N. Sun), david.letouze@ec-nantes.fr (D. Le Touzé), zhangaman@hrbeu.edu.cn (A.-M. Zhang).

1 Introduction

In the ocean engineering field, many hydrodynamic problems with free surface and viscous effects have been well resolved by potential-flow solvers or different mesh-based computational-fluid-dynamics(CFD) solvers. However, for those numerical solvers, the modeling of complex Fluid-Structure-Interaction (FSI) problems with strong fluid impacts, considerable structure displacements/deformations and violent multi-fluid mixing, still represents a great challenge. As the growing demand from the industry for solving these highly complex FSI problems, particle-based numerical methods are rapidly growing in recent years [15].

Particle methods were born for continuum mechanical problems with large interface or boundary deformations [32, 55]. In the field of fluid dynamics, Smoothed Particle Hydrodynamics (SPH) method, as a representative, has been successfully applied for the free-surface ([4, 34]) and multi-phase ([56, 17]) flows under some quite challenging and complex flow conditions, some of which are in large scale and towards the industrial applications ([43, 57]) when the technique of high performance computing is adopted for efficient parallel computations [41, 12].

In most cases, the single-phase SPH model is directly applied for the modeling of free-surface flows under moveable wall boundaries and ignoring the air-phase effects. This simplification is similar to the numerical computation using a potential flow solver, in which the pressure on the free surface is zero and the space above the free surface is assumed as vacuum. Colagrossi et al. [9] theoretically proved this single-phase simplification is consistent on the free surface even though the kernel truncation occurs there. However, this simplification is true only when the free surface deformation is small. In fact, when the free-surface rolling occurs in nature, the entrapped air-bubble under the free-surface starts to be dominant and the vacuum assumption is no more tenable. Accurately taking into account the air-phase effects in complex multi-phase flows still represents a big challenging issue for both mesh-based and particle-based numerical methods.

For mesh-based numerical methods, the interface-tracking using different numerical techniques (*e.g*. Level-Set, Volume of Fluid, etc.) still faces many stability and conservation problems in some complex multi-phase flows. On the contrary, as was demonstrated in [17], the multi-phase SPH model has demonstrated superior capability in dealing with complex interfacial flows with large density and viscous ratios, showing clear and sharp interface evolutions and maintaining the exact mass conservation. As has been recently pointed out by Marrone et al. [37] in some featured SPH simulations, entrapped air-bubbles in the cavity after the water entry of objects, or after the wave rolling and breaking, paly a significant role in the overall flow evolution and further lead to non-negligible effects on the load to the structure. Unfortunately, in [37], the effect of the structure's elastic-response, which is anther important factor affecting the flow evolution and hence the impact load, was not

discussed. In fact, thanks to the mesh-free characteristics of the particle method, large structure deformations can also be straightforwardly modeled in the same particle-framework.

So far, there are many particle-based numerical schemes (*e.g.*, SPH [11, 49], Incompressible SPH (ISPH)[44], Moving Particle Semi-implicit (MPS) method [25], Finite Particle Method (FPM)[60], etc.) and coupled solvers (*e.g.*, SPH-SPH [3, 18] SPH-FEM [14], MPS-FEM [58], ISPH-SPH [22], Dual Particle Dynamics-MPS (DPD-MPS) [13], etc.) reported in the literature for FSI problems. However, most of them are limited within the scope of a single-phase fluid solver coupled with a structure solver while the air-phase effects have rarely been taken into account. To fill this gap, a FSI-SPH model will be established and applied in this paper towards the complex multi-phase FSI problems. The accurate tracking of the multi-phase interface and the fluid-structure interface in the pure-Lagrangian framework of the present SPH method is more straightforward and therefore maintains higher accuracy.

On the other hand, in addition to pursuing a satisfied numerical accuracy, the computational efficiency is another factor which should be emphasized. For example in the ocean engineering field, the structure thickness is usually very thin and therefore very fine particle resolution is necessary to accurately discretize the structure into sufficient number of particles if no thin-plate assumption is considered. In that case, a proper multi-resolution numerical solver is required in order to ensure a high local-accuracy near the structure surface while de-refine the particle resolution in the far field and hence reduce the total computational effort.

In the literature, there are a variety of multi-resolution techniques for particle methods, including the techniques of particle splitting-merging [53, 54] or overlapping [8, 45]. However, to our knowledge, very few of these techniques have been applied for multi-phase FSI flows. Recently, in [21, 25], the authors proposed to adopt a multi-resolution particle method in the framework of MPS to model FSI problems. In their treatment, different particle resolutions are imposed for the structure and fluid respectively, which allows to locally improve the particle resolution for the structure; however, in some cases in order to improve the accuracy of the hydrodynamic force, the refinement for the fluid particles in a local region near the structure is also necessary. Therefore, to develop a multi-resolution solver for both the fluid and structure portions is required. On the other hand, when applying multi-resolution techniques for the simulation of multi-phase flows, we need to ensure that, at the intersection of multi-phase and multi-resolution interfaces, numerical accuracy and stability are equivalent as in the region of single-phase and single-resolution. That brings the necessity of the accurate extension and rigorous validation of the existing multi-resolution techniques from single-phase flows to multi-phase flows.

In the present work, we introduce a coupled FSI-SPH solver by combining a multi-

phase δ-SPH scheme for complex multi-phase flows and a Total-Lagrangian Particle (TLP) solver [29] for elastic structures. Although the well-known δ-SPH scheme has been developed for a decade, and has been widely applied for many hydrodynamic problems [39, 50, 51], its direct application to free-surface flows considering air-phase and FSI effects with large structural deformations are still rarely reported in the literature. Therefore, firstly we extend the classic δ-SPH scheme to the multi-phase context allowing the density ratio between the denser and lighter phases up to the order of 1000. Further, the Adaptive Particle Refinement (APR) technique, originally proposed by [6] and enhanced by [8], is extended for the modeling of multi-phase flows in order to obtain higher local accuracy but achieve a significant reduction of the total computational effort.

The multi-phase and multi-resolution δ-SPH scheme is then coupled to the TLP method, which comes into being the FSI-SPH model for multi-phase FSI problems. Thanks to the Lagrangian kernel as adopted in the TLP method (see [29]), tensile instability is well avoided in the structure part. However, for the fluid solver, despite of the adoption of the Eulerian kernel function in the SPH method, the technique of Tensile Instability Control (TIC) [45] has to be adopted to prevent the occurrence of the fluid fragmentation in the regions characterized by negative pressure.

Regarding the numerical results, for the multi-phase FSI problems relevant to ocean engineering applications, there is still a lack of representative benchmarks with both experimental data and reliable numerical solutions by both mesh-based and particle-based numerical methods. Therefore, in this work, we present a comprehensive SPH simulation of the series test-cases of the dam-breaking flow impacting the elastic plate [28] and carefully validating the numerical results. With the robust mesh-free FSI-SPH solver, for these complex FSI problems, some important phenomena will be thoroughly analyzed. Moreover, the mechanical mechanism behind those physical phenomena will also be discussed.

The present paper is organized as follows. Section 2 will firstly give a brief introduction about the multi-phase and multi-resolution δ-SPH scheme, and then the TLP method and the coupling algorithm between the SPH and TLP methods are presented. Section 3 consists of all the numerical results where comparative investigations for the SPH model and related numerical aspects are carried out and after that sufficient validations and analyses for the multi-phase FSI problems will be presented. Conclusions and future perspectives will be given in the last part of the paper.

2 Multi-phase and multi-resolution Lagrangian model for FSI problems

In the simulation of multi-phase FSI problems using the present particle method, the whole computational domain is discretized into Lagrangian particles whose

quantities are evolved by solving different governing equations belonging to the fluid or structure. The fluid part, which is consist of water and air particles, is solved by the multi-phase δ-SPH scheme with different equations of state for water and air, see Section 2.1; while the structure part, discretized by solid particles, is solved by the TLP method, see Section 2.2. The algorithm for coupling the fluid and structure solvers will be presented in Section 2.3. The boundary of the whole flow is modeled by fixed ghost particles whose variables are extrapolated form the inner flow. The Lagrangian nature of the pure particle method allows for the convenient and accurate handling of the interfacial flows with strong material convection and large boundary deformations.

2.1 Extension of the δ-SPH scheme to the multi-phase context

The δ-SPH scheme [5] is a SPH variant developed based on the classic SPH scheme of Monaghan [40]. The main characteristic for δ-SPH is the δ-term added in the continuity equation for preventing the high-frequency pressure oscillation. δ-SPH scheme was initially proposed for the simulation of single-phase free-surface flows and, therefore, when it is applied for multi-phase flows, some modifications regarding to the multi-phase interface and the stability of the air-phase are necessary, see more in the following subsections.

2.1.1 Governing equations for the multi-phase δ-SPH scheme

The governing equations for the multi-phase δ-SPH scheme are written as [5, 34]

$$\begin{cases} \dfrac{D\rho_i}{Dt} = -\rho_i \displaystyle\sum_j (\boldsymbol{u}_j - \boldsymbol{u}_i)\cdot\nabla_i W_{ij} V_j + \delta\, h_i\, c_{0i} \sum_j \mathcal{D}_{ij}\cdot\nabla_i W_{ij} V_j\,, \\ \dfrac{D\boldsymbol{u}_i}{Dt} = -\dfrac{1}{\rho_i}\displaystyle\sum_j \mathcal{F}(p_j,p_i)\nabla_i W_{ij} V_j + \boldsymbol{g}_i + \dfrac{\alpha h_i c_{0i}\rho_{0i}}{\rho_i}\sum_j \pi_{ij}\nabla_i W_{ij} V_j + \dfrac{1}{\rho_i}F_i^{interface}\,, \\ \dfrac{D\boldsymbol{x}_i}{Dt} = \boldsymbol{u}_i\,, \\ p_i = \dfrac{c_{0i}^2\rho_{0i}}{\gamma_i}\left(\dfrac{\rho_i}{\rho_{0i}} - 1\right)^{\gamma_i} + p_b\,, \qquad V_i(t) = \dfrac{m_i}{\rho_i(t)}\,. \end{cases} \tag{1}$$

In the above equations, the mass, density, volume, pressure, velocity and position of the i-th particle are denoted by notations as m_i, ρ_i, V_i, p_i, $\boldsymbol{u}_i$ and $\boldsymbol{x}_i$, respectively. $\boldsymbol{g}$ is the vector representing the body force which is the gravitational force in the present work. From the last equation, we can see that the mass of each particle is a constant while the particle density and volume are variables in time. The notation $W_{ij} = W(|\boldsymbol{x}_i - \boldsymbol{x}_j|; h)$ represents the kernel function for which the Wendland C2 kernel has been adopted in this work. The smoothing length $h_i/\Delta x_i = 2$ has been

adopted with Δx_i being the initial particle spacing.

The velocity divergence in the continuity equation is approximated by using the particle approximation based on the kernel interpolation theory [32]. Differently to the traditional SPH approximation of the pressure gradient where the conservative form $\mathcal{F}(p_j, p_i) = (p_i + p_j)$ is usually adopted, in the present work, in order to completely prevent the so-called tensile instability, a TIC technique [45] has been adopted. Finally, $\mathcal{F}(p_j, p_i)$ is written as

$$\mathcal{F}(p_j, p_i) = \begin{cases} p_j + p_i\,, & p_i \geq 0 \quad \text{or} \quad i \in S_F\,, \\ p_j - p_i\,, & p_i < 0 \quad \text{and} \quad i \notin S_F\,, \end{cases} \tag{2}$$

where S_F stands for the free-surface region which is consist of all the free-surface particles and their neighboring particles (see [48]). However, for the multi-phase simulations in this paper, since above the denser phase (water), air particles are distributed and closed by the wall boundary and therefore the free-surface region does not exist. The TIC is able to completely prevent the tensile instability (behaving as the fluid fragmentation or flow voids) when the pressure becomes negative, however it leads to the non-conservation of the total momentum since the pressure gradient operator is no more anti-symmetric. Fortunately, this drawback can be remitted when the particle distribution is uniform [45].

Differently to the wide implementation of the Particle Shifting Technique (PST) (see [31]) in a variety of particle models and applications (see *e.g.* [45, 59, 23, 46]), in this work, instead of PST we add a constant background pressure p_b in the equation of state to regularize the particles' distribution. The mechanism of the constant pressure for regularizing particles has been analyzed in [10]. For the dam-breaking test cases in the present work, the magnitude of p_b is explicitly defined as

$$p_b = \frac{1}{2}\rho_0 U^2; \quad U = \sqrt{gH}, \tag{3}$$

where ρ_0 is the reference density when the pressure is zero, $g = 9.81 m/s^2$ is the magnitude of the gravity acceleration and H stands for the initial water depth. p_b is particularly effective in regularizing the distribution of the light particles (the air-phase) in the multi-phase SPH simulations. On one hand, it reduces the non-conservation of momentum caused by the TIC term; On the other hand, it ensures the stability of the light particles under violent fluid impacts in the multi-phase simulation when the density ratio is up to 1000.

We note that a moderate value of the magnitude of p_b is defined here aiming to, in some extent, reduce the unfavorable effects associated with application of the background pressure. As has been stated in Adami et al. [2], spurious pressure gradients can be induced by p_b. In addition, Khayyer et al. [24] also found that the background pressure adversely affects the overall energy conservation property in the particle method. Indeed, the TIC term allows the existence of negative pressure

in the flow flied and therefore using a large p_b to get rid of all the negative pressure is no more mandatory in the present SPH method. Finally, the moderate value of p_b defined in Eq. (3) works properly, at least for the test cases in the present work.

In addition, in the equation of state the artificial sound speed c_i for the different phases has to be determined carefully. On one hand, the density variation should satisfy the weakly-compressible hypothesis (within 1%, see [40]); on the other hand, c_i should be able to maintain the continuity of the pressure/normal-velocity at the multi-phase interface [11]. In order to satisfy the weakly-compressible hypothesis, the constant sound speed c_w for the water part is determined by [48]

$$c_w \geq 10\max\left(U_{\max}, \sqrt{p_{\max}/\rho_{0w}}\right), \tag{4}$$

where $U_{\max}$ and $p_{\max}$ are the maximum expected velocity and pressure in the water region. In addition, $\gamma_w = 7$ is adopted for all the water particles. While for the lighter phase (i.e. air particles in this work), a smaller γ_a equals to 1.4 is assigned for the purpose of a steeper density-pressure characteristic curve, see more in [11]. Through $c_w^2\rho_{0w}/\gamma_w = c_a^2\rho_{0a}/\gamma_a$, we can obtain the sound speed c_a for the air phase based on the sound speed c_w in the water phase as

$$c_a = \sqrt{\frac{c_w^2\gamma_a\rho_{0w}}{\gamma_w\rho_{0a}}}. \tag{5}$$

We underline that the above derivation for obtaining the artificial sound speed is based on a compromise between the accuracy, efficiency and stability, but for the specific dam-breaking problem in the present work, the sound speed obtained for the air phase using the above process is close to the physical one, which provides a proper estimation for the compressibility in the air cavity, see more in Section 3. Another way to strictly consider the physical compressibility of the air phase is to exactly use the physical sound speed for air (see, e.g., [37]), and based on that using Eq. (5) one can obtain the sound speed in water. However, in some cases one possibility could be the sound speed obtained for water in this way is too low, in other words, doesn't satisfy the weakly compressible hypothesis (i.e. Eq.(4)). As a remedy, the compressible-incompressible multi-phase particle scheme proposed by Khayyer and Gotoh [20] or the one proposed by Lind et al. [30] can be applied to solve this problem.

In system (1), the forms of the diffusive term $\mathcal{D}_{ij}$ and the viscous term π_{ij} are written as [5]

$$\mathcal{D}_{ij} = \begin{cases} 2\left[\left(\rho_j - \rho_i\right) - \frac{1}{2}\left(\langle\nabla\rho\rangle_i^L + \langle\nabla\rho\rangle_j^L\right)\cdot\boldsymbol{x}_{ji}\right]\frac{\boldsymbol{x}_{ji}}{\|\boldsymbol{x}_{ji}\|^2}, & i,\ j \in \text{same phase}, \\ 0, \quad \text{otherwise}, \end{cases} \tag{6}$$

and

$$\pi_{ij} = \begin{cases} 2(d+2)\dfrac{\left(\boldsymbol{u}_j - \boldsymbol{u}_i\right)\cdot\left(\boldsymbol{x}_j - \boldsymbol{x}_i\right)}{\|\boldsymbol{x}_{ji}\|^2}, & i,\ j \in \text{same phase}, \\ 0, \quad \text{otherwise}, \end{cases} \tag{7}$$

where $\boldsymbol{x}_{ji} = \boldsymbol{x}_j - \boldsymbol{x}_i$, d is the spacial dimension and the density gradient $\langle\nabla\rho\rangle^L$ is evaluated using the renormalized spatial gradient (see *e.g.* [42]) as

$$\begin{cases} \langle\nabla\rho\rangle_i^L := \displaystyle\sum_{j\in\chi_i}\left(\rho_j - \rho_i\right)\mathbb{L}_i\nabla_i W_{ij}V_j, \\ \mathbb{L}_i := \left[\displaystyle\sum_{j\in\chi_i}\left(\boldsymbol{x}_j - \boldsymbol{x}_i\right)\otimes\nabla_i W_{ij}V_j\right]^{-1}, \end{cases} \tag{8}$$

where χ_i denotes all the neighboring particles that belong to the fluid of the ith particle.

The parameters of $\delta = 0.1$ and $\alpha = 0.1$ are adopted in the diffusive terms to stabilize the simulation (see for details in [5]). According to the investigation as carried out by Marrone et al. [36], a moderate numerical dissipation is necessary in the initial stage of the fluid impact in order to filter the elastic energy and recover to the incompressible solution.

In order to keep the sharpness of the multi-phase interface, the interface sharpness force $F_i^{interface}$ has been added into the momentum equation. The expression of $F_i^{interface}$ is written as [16]

$$F_i^{interface} = -0.08\sum_{j\in\chi_i^C}(\|p_j\| + \|p_i\|)\nabla_i W_{ij}\,V_j\,, \tag{9}$$

where χ_i^C denotes all the neighboring particles that do not belong to the fluid of the ith particle. The interface sharpness force is effective in preventing the interface penetration, however it leads to a slight gap between different fluid phases. To overcome this side-effect, in the framework of the MPS method, a conservative density smoothing technique [19] was proposed and showed an clear improvement on eliminating the unphysical gap.

Lastly, the forth order Runge-Kutta integration scheme is adopted in this work to match the governing equations in time with the CFL number as 1.25 for determining the time step, see more in [5, 7].

2.1.2 Extension of APR to multi-phase flows with a phase-switch correction

In the present work, in order to improve the local accuracy around the structure and accelerate the computational speed, the technique of Adaptive Particle Refinement (APR) [6] has been implemented. In this technique, one coarse particle (also called mother particle) which enters the splitting domain will be split into 4 (2D) or 8 (3D) refined particles (also called daughter particles). The mother particles are switched to be inactive after splitting and the generated daughter particles become active and join in the SPH calculation (Eqs. (1)). The inactive mother particles are transported in a purely Lagrangian manner by interpolating the velocity from the background flow (formed by refined/daughter particles which are active) and are reactivated after they flow out of the splitting domain. The daughter particles which flow out of the splitting domain are simply deleted from the particle system. Note that, on the interface between different particle levels, an extension of the splitting domain (named as the translational domain in [6] and the guard zone in [8]) is needed to fulfil the kernel function for the daughter particles and the activity of the mother and daughter particles in the translational/guard zone is opposite with respect to the one inside the splitting domain, see more in [8].

The key idea in the APR technique is how to exchange/couple the flow information on the interface of different levels of particle resolutions. In the original work of [6], a transitional domain with a predefined weight function is adopted to couple the different particle levels. The second version of the APR proposed in [8] used an interpolation formulation using a Shepard kernel function to exchange the flow variables between different resolution levels (in other words, between active and inactive particles) and the latter is adopted and extended to the multi-phase flows in this paper. A limitation of this technique is that the distribution of the inactive particles can be disordered due to their purely Lagrangian motions by interpolating the velocity from the background velocity field (see also in [51]), therefore as a remedy, a particle shifting technique has been applied to all the inactive particles in this work.

Indeed, in the previous literature ([6] and [8]), the APR has only been applied to single-phase flows with rigid wall boundaries. When applying this technique to multi-phase flows, some additional numerical modifications are necessary. As stated in the last subsection, some key flow variables on the multi-phase interface, for example the density or mass, are discontinuous; while the pressure, normal velocity are always continuous. The discontinuity of these variables on the interface brings the challenge for the coupling of different levels of particle resolutions. One solution is to simply restrict that the inactive particles can only interpolate the variables from the surrounding active particles of the same phase. However, this simple solution brings some instability when the number of neighboring active particles from the same phase is limited, for example on the tip of the splashing jet.

Instead, we propose an interpolation-correction algorithm to tackle this problem.

In this algorithm, firstly, since the pressure is continuous, we can directly use the following Shepard kernel to interpolate the pressure [8],

$$\phi_{i\in inactive} = \sum_{j\in SPH} \phi_j W_{ij} \Big/ \sum_{j\in SPH} W_{ij}, \tag{10}$$

where ϕ stands for a general flow variable like pressure. We note that the particle indexed by j comes form all the active neighboring particles from the other resolution level. Based on the interpolated pressure, the particle density can be obtained through the equation of state in Eqs. (1).

In the present work, we neglect the slip motions between different fluid phases on the multi-phase interface, so we can make an compromise to interpolate all the velocity components also using Eq. (10), but this leads to the nonphysical interpolation of the velocity in the case when an inactive particle's neighboring active particles are all from a different phase. More specifically, this situation mainly occurs for the refined particles which are transported into the guard zone (become inactive), while the coarse inactive particles from a lower resolution are not able to follow these refined particles (limited by the coarse resolution). In that circumstance, the refined inactive particle is possible to completely inherit the velocity from the active particles which are all from the different phase. For instance, the fluid jet or droplet should not inherit the velocity from the surrounding air flow whose velocity is completely different to the velocity inside the droplet due to the large density difference.

Therefore, if an inactive particle can not find at least one active particle of the same phase within its kernel support, a correction step is added to switch the type of the inactive particle to be the same as the surrounding active particles. As stated before, our phase-switch correction can avoid the droplet particles to inherit the air velocity and to validate this, a numerical test will be presented in Section 3.2. Since the phase-switch correction is only implemented for the inactive particles, the side effect on the mass conservation for all the active particles is not a main issue.

2.1.3 Boundary conditions

The "Fixed Ghost Particle" technique presented in [34] is implemented in this work to model all the solid wall boundaries. Free-slip boundary condition is enforced for all the non-penetration surfaces, including the rigid wall and the elastic structure. The viscous force is simply switched to zero in a particle pair which consists of a fluid particle and a ghost particle and this simple treatment removes all the frictional force from the ghost particle. The fluid variables are extended to the ghost particles by an extrapolation using the Shepard interpolating formula similar to Eq. (10), for more details the readers can also refer to [50, 1].

Differently to the δ-SPH method for the fluid solver, in the Total Lagrangian Particle (TLP) method, only the momentum equation is solved. Through the constitutive relationship, the stress tensor is linked to the strain tensor which is based on the structure deformation with respect to its initial configuration. Therefore, the solving of the continuum equation for the density of the solid particle is not necessary. Further, a Lagrangian kernel is adopted for the particle approximation which means through out the simulation, the kernels and their gradients are all evaluated with respect to the initial particle configuration and therefore the numerical instability caused by the irregular particle distribution is avoided. The momentum equation for the TLP method is written as [29]

$$\frac{D\boldsymbol{u}}{Dt} = \frac{1}{\rho_0^s}\nabla_0 \cdot \boldsymbol{P} + \boldsymbol{g}, \tag{11}$$

where $\boldsymbol{u}$ is the velocity of the solid particle and ρ_0^s is the particle's density being a constant in time. $\nabla_0 \cdot \boldsymbol{P}$ denotes the divergence of the stress tensor with subscript 0 indicating a Lagrangian kernel will be used in the particle approximation. More specifically, $\boldsymbol{P}$ is the first Piola-Kirchhoff stress tensor and can be written using the Cauchy stress tensor $\boldsymbol{\sigma}$ as [29]

$$\boldsymbol{P} = \det(\boldsymbol{F})\boldsymbol{\sigma}\boldsymbol{F}^{-\mathrm{T}}; \quad \boldsymbol{F} = \frac{d\boldsymbol{x}}{d\boldsymbol{X}}, \tag{12}$$

where $\boldsymbol{F}$ is the tensor of the deformation gradient. $\det(\boldsymbol{F})$ indicates the determinant of $\boldsymbol{F}$ and the superscript $-\mathrm{T}$ stands for the inverse of the transposed tensor. The vector $\boldsymbol{x}$ stands for the current particle position and $\boldsymbol{X}$ refers to its initial reference position. In order to avoid the numerical error caused by the truncated kernel function on the structure surface, the deformation matrix can be written using the renormalized kernel approximation as [47]:

$$\begin{cases} \boldsymbol{F}_i = \left\langle \dfrac{D\boldsymbol{x}}{D\boldsymbol{X}} \right\rangle_i = \displaystyle\sum_j \left(\boldsymbol{x}_j - \boldsymbol{x}_i\right) \otimes \boldsymbol{M}_{0i} \nabla_{0i} W_{0ij} V_{0j} \\ \boldsymbol{M}_0\left(\boldsymbol{X}_i\right) = \left[\displaystyle\sum_j \left(\boldsymbol{X}_j - \boldsymbol{X}_i\right) \otimes \nabla_{0i} W_{0ij} V_{0j} \right]^{-1}, \end{cases} \tag{13}$$

where V_0 is the particle volume which is a constant as the particle mass and density. Note that the kernel function and its gradients are all evaluated based on the initial particle configuration as the subscript 0 has indicated.

Regarding to the Cauchy stress tensor $\boldsymbol{\sigma}$, in two dimensions, $\boldsymbol{\sigma}$ can be expanded as

[29]

$$\begin{bmatrix} \sigma^{11} \\ \sigma^{22} \\ \sigma^{12} \end{bmatrix} = \frac{E_s}{1-{\nu_s}^2} \begin{bmatrix} 1 & \nu_s & 0 \\ \nu_s & 1 & 0 \\ 0 & 0 & (1-\nu_s)/2 \end{bmatrix} \begin{bmatrix} \varepsilon^{11} \\ \varepsilon^{22} \\ 2\varepsilon^{12} \end{bmatrix}, \tag{14}$$

where E_s and ν_s are the Young's modulus and the Poisson's ratio, respectively. The Euler strain tensor $\boldsymbol{\varepsilon}$ can be written as [29]

$$\boldsymbol{\varepsilon} = \boldsymbol{F}^{-\mathrm{T}} \boldsymbol{E} \boldsymbol{F}^{\mathrm{T}}; \quad \boldsymbol{E} = \frac{1}{2}\left[\boldsymbol{L} + \boldsymbol{L}^{\mathrm{T}} + \boldsymbol{L}^{\mathrm{T}}\boldsymbol{L}\right], \tag{15}$$

where $\boldsymbol{E}$ is the Green-Lagrange strain tensor and $\boldsymbol{L}$ is the displacement gradient tensor written as [29]

$$\boldsymbol{L} = \frac{d\boldsymbol{v}}{d\boldsymbol{X}}, \tag{16}$$

where the displacement vector is $\boldsymbol{v} = \boldsymbol{x} - \boldsymbol{X}$. Similar to Eq. (13), $\boldsymbol{L}$ is also discretized by the renormalized kernel approximation [47] as

$$\begin{cases} \boldsymbol{L}_i = \left\langle \dfrac{D\boldsymbol{v}}{D\boldsymbol{X}} \right\rangle_i = \displaystyle\sum_j \left(\boldsymbol{v}_j - \boldsymbol{v}_i\right) \otimes \boldsymbol{M}_{0i} \nabla_{0i} W_{0ij} V_{0j} \\ \boldsymbol{M}_0\left(\boldsymbol{X}_i\right) = \left[\displaystyle\sum_j \left(\boldsymbol{X}_j - \boldsymbol{X}_i\right) \otimes \nabla_{0i} W_{0ij} V_{0j}\right]^{-1}. \end{cases} \tag{17}$$

Based on Eq. (13) and Eq.(17), the discrete form of the first Piola-Kirchhoff stress tensor $\boldsymbol{P}$ can be obtained and then substituting it into Eq. (11) yields the discretized momentum equation where, in order to maintain the exact conservation of the momentum, the classic anti-symmetric SPH approximation is adopted for the divergence operator. In addition, the artificial viscosity is also added into the momentum equation for the stability purpose. Finally, similar to [29] the discrete momentum equation is

$$\frac{d\boldsymbol{u}_i}{dt} = \frac{1}{\rho_0^s} \sum_j \left(\boldsymbol{P}_i + \boldsymbol{P}_j + \boldsymbol{P}_{vij}\right) \cdot \nabla_{0i} W_{0ij} V_{0j} + \boldsymbol{g}_i, \tag{18}$$

where the artificial viscous force $\boldsymbol{P}_{vij}$ exerted by the particle j on the particle i is written as [29]

$$\begin{cases} \boldsymbol{P}_{vij} = \det(\boldsymbol{F}_i) \prod_{ij} \boldsymbol{F}_i^{-\mathrm{T}} \\ \prod_{ij} = \alpha_s c_s h_s \rho_0^s \dfrac{(\boldsymbol{u}_j - \boldsymbol{u}_i) \cdot (\boldsymbol{x}_j - \boldsymbol{x}_i)}{\left|\boldsymbol{x}_j - \boldsymbol{x}_i\right|^2 + (0.01 h_s)^2}. \end{cases} \tag{19}$$

The artificial viscosity converges to zero as the increase of the particle resolution ($h_s \to 0$). In this work, the coefficient α_s for all the solid particles is set as 0.2. A small ratio as $h_s/\Delta x = 1.3$ between the smoothing length h_s of the solid particles and their initial particle spacing Δx is used in this work since the smaller ratio has

been shown to be more effective in preventing the particle clumping under large structure deformations.

The momentum equation is integrated in time using the 4^{th} order Runge-Kutta scheme as in the fluid part. The time step $\Delta\hat{t}_s$ for the TLP method is determined as [29]

$$\Delta\hat{t}_s = 0.8\frac{h_s}{c_s}; \quad c_s = \sqrt{K_s/\rho_0^s}, \tag{20}$$

where c_s is the sound speed in the structure and K_s is the bulk modulus which can be written as $K_s = E_s/[3(1-2\nu_s)]$.

The fixed boundary condition for the structure solver is implemented in a similar manner as the "Fixed Ghost Particle" for the fluid part. However, instead of using an extrapolation formula to update the variables of the ghost particles, in the TLP method when simulating a fixed boundary, the ghost particles are simply fixed on their initial positions with their velocities frozen to be zero and the other variables are updated according to the governing equation of the structure.

2.3 Coupling between the multi-phase δ-SPH scheme and TLP method for FSI problems

The elastic structure is discretized into solid particles which, on one hand serve for simulation of the elastic response of the structure, and on the other hand serve as the "Fixed Ghost Particle" to enforce the non-penetration boundary condition for the SPH simulation. As derived by [7] , the forces on the solid particles can be measured by summating the interacting forces between the fluid particles and the solid/ghost particles as

$$\boldsymbol{F}_{j\in solid} = -\sum_{i\in fluid}\left[-(p_j+p_i)+\alpha h_i c_{0i}\rho_{0i}\pi_{ij}\right]\nabla_i W_{ij} V_i\, V_j. \tag{21}$$

In Eq.(21), the pressure p_j for the solid/ghost particles (denoted by the subscrit j) are extrapolated from fluid particles (denoted by the subscript i) satisfying the non-penetration condition, see more details in [34] and [1].

The fluid solver δ-SPH scheme is coupled with the TLP method using the sequential staggered algorithm [14], allowing for a sufficient numerical stability when the mass ratio between the structure and the fluid is small. In the FSI solver, the acceleration of the solid particles is computed by taking into account three force components with the first and second components in Eq. (18) which includes the inner forces ($\boldsymbol{P}$ and $\boldsymbol{P}_v$), the external body force $\boldsymbol{g}$ (*e.g.* gravitational force) and the third component $\boldsymbol{F}$ exerted by the interacting fluid particles (see Eq. (21)).

As the TLP method is explicit, its time step is strictly limited by the bulk modulus

of the elastic structure. Since the sound speed in the structure is significantly larger than the artificial sound speed in the weakly compressible SPH method for the fluid, the time step in TLP method is much smaller than the one in δ-SPH. In order to match the δ-SPH and TLP in an efficient manner, a step-substep coupling technique has been adopted. That means, within one time step of the fluid evolution, the structure part can step forward continuously in several time steps, until arriving at the same time instant of the fluid part. The step-substep coupling technique allows an equilibrium accuracy with respect to the traditional step-step coupling, but avoids repeated calculations in the fluid part with a much smaller time step than the one derived by it's own CFL condition. Finally, since the fluid and structure solvers are both established in the particle framework, many subroutines can be shared between each other, which contributes to much convenience in the parallel computing and increases the numerical efficiency.

3 Numerical investigations

Before applying the FSI-SPH model to a complex fluid-structure interaction problem, the rigorous and comprehensive validations in terms of stability, accuracy and conservation properties with some basic benchmarks are necessary. Some typical benchmarks for validating the structure solver and the fluid-structure coupling solver can be found in [22, 14, 52]. In Appendix A, based on the test of the dynamic response of an oscillating plate in the gravity field, we have validated the accuracy of the structure solver. Further, since the simulation of the hydrostatic water on an elastic plate as carried out in [22, 14, 26] is crucial for assessing the property of stability-preserving of the FSI coupling algorithm, in Appendix B, the hydrostatic test is carried out and the numerical result by the present FSI-SPH model has shown good agreement with the analytical solution when a sufficient particle resolution is adopted. After these validations using the basic benchmarks, in the following sections, more complex FSI dam-breaking problems will be modeled and reference results including the experimental data by Liao et al. [28] will be adopted to validate the numerical results.

3.1 Dam-breaking flow impacting an elastic plate: the problem description

Indeed, the classic dam-breaking benchmark test (see *e.g.* [33]) has been widely adopted to test the performances of different mesh/particle based numerical solvers. Generally two factors in the dam-breaking flow are concerned by the researchers, respectively the impact pressure and the effect of the entrapped air-bubble after the rolling-down of the water tongue on the underlying free-surface. However, the FSI effect has not been considered in the classic dam-breaking experiment [33] and therefore, it is necessary to further extend this classic test to a more comprehen-

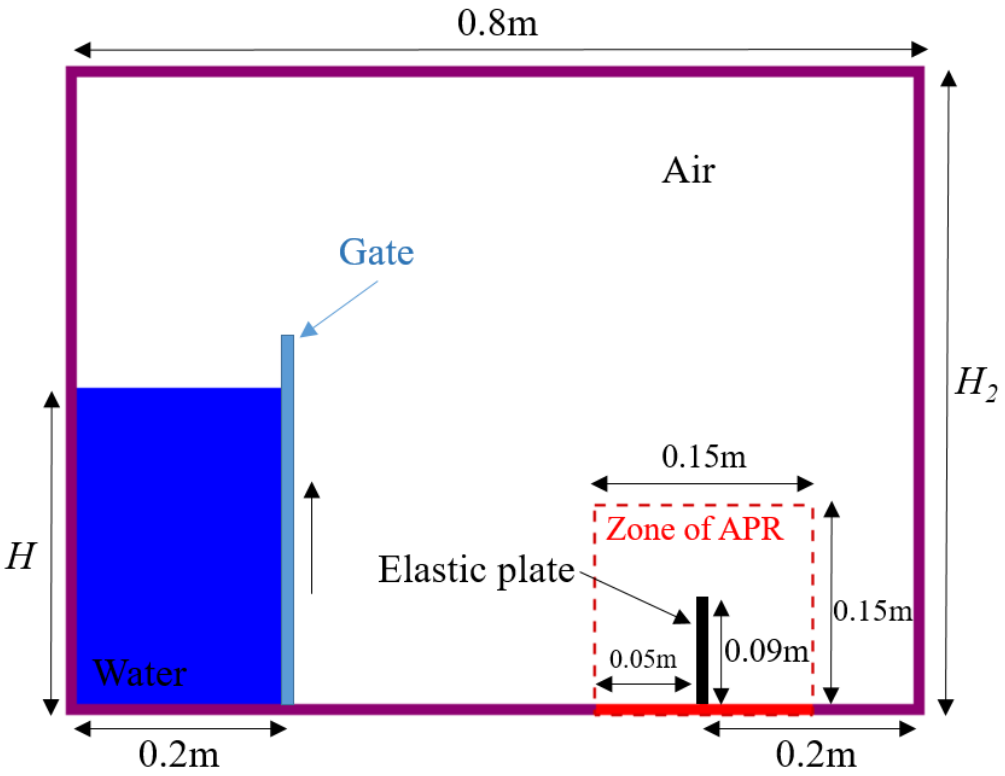

Fig. 1. Illustration for the initial condition in the experiment and the present SPH simulation of the dam-breaking flow impacting the elastic plate [28].

sive three-phase-coupling context which specifically refers to the liquid-gas-elastic coupling.

Thanks to the experiment conducted by Liao et al. [28], good experimental data is available, however, most of the numerical study after the publishing of this experiment is still restricted to either the single-phase simulation or the multi-phase study but within a short duration (before the collapsing of the air cavity). Although Liao et al. [28] carried out a long-time simulation by using their FDM-FEM coupling technique, as restricted by the free surface detection technique in an Eulerian solver, the sharpness of the air-water interface is adversely affected by the mesh resolution adopted in their study. As the SPH method has been quite popular for the FSI problems with the large boundary deformation and multi-phase mixing, the Lagrangian particle method introduced in the previous section is employed to simulate the series experiments of Liao et al. [28], in order to seek more flow details and reveal more features during those complex FSI phenomena and therefore provide more reference for the future numerical validations of the other CFD solvers.

The sketch for the dam-breaking experiment and numerical simulation is depicted in Figure 1. A water column with the initial depth denoted as H is stored on the left side of the tank which is $0.8m$ in length and H_2 in height ($H_2 > H$). The water column is initially blocked with a water gate which can rise up to form the dam-breaking flow. The APR zone with a side-length as $0.15m$ in Figure 1 denotes the

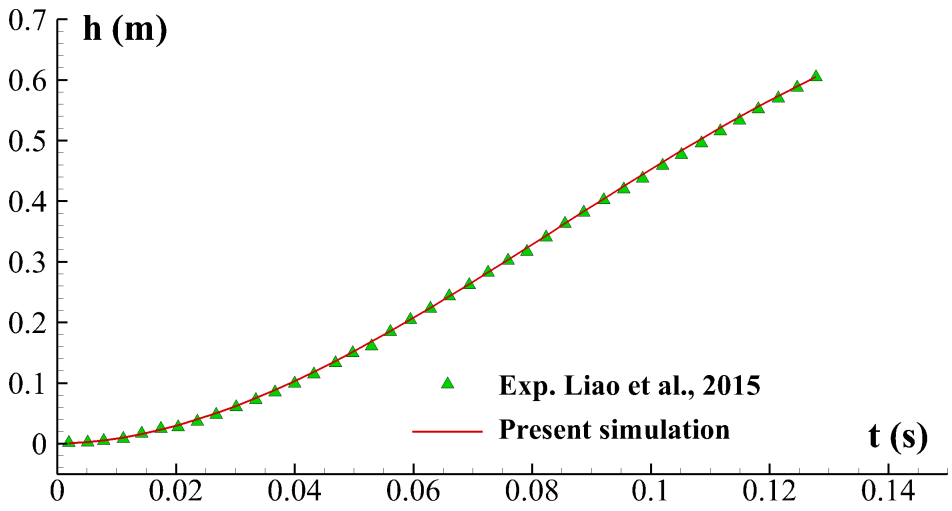

Fig. 2. Rising-up law of the gate in the dam-breaking experiment [28] and the present SPH simulation.

splitting zone which means the particles entering this zone will be refined into a doubled resolution, improving the local accuracy for evaluating the impact load on the structure.

In all the numerical simulations of this paper, the water density is $\rho_w = 997.0\,kg/m^3$ and the density ratio between water and air is assumed to be 1000. The density of the elastic plate made of rubber is $\rho_s = 1161.54\,kg/m^3$, the Young's modulus is $E_s = 3.50\,MPa$ and the Poisson's ratio is $\nu_s = 0.45$.

After a gradual lift-up of the gate by the pulley mechanism, the water column collapses and the formed water tongue impacts the bottom-fixed elastic plate which is $0.2m$ far from the vertical tank wall on the right side. As emphasized by Liao et al. [28], the shape of the water front of the dam-breaking flow is sensitive to the gate motion. Therefore, conversely to the classic SPH modeling of the dam-breaking flow in the literature (see *e.g.* [34]), here the effect by the gate motion is also considered. According to the experiment of Liao et al. [28], we interpolate the displacement of the gate bottom from the experimental data and obtain a spline curve which is expressed as

$$h_g(t) = -285.115t^3 + 72.305t^2 + 0.1463t, \tag{22}$$

where $h_g(t)$ stands for the time evolution of the height of the bottom end of the gate. The comparison between the spline curve (Eq.(22)) used in the SPH simulation and the experimental data is plotted in Figure 2.

After the release of the water gate, the water tongue is formed and impacts the plate. The water firstly bends the elastic plate and then flows over it and impacts the vertical tank wall. After that an air bubble is entrapped among the tank wall, the

elastic plate and the water flow. The horizontal displacements of three markers on the middle line of the elastic plate with different initial heights are recorded in the experiment and simulation and provide a quantitative reference for the validation of numerical solvers. The three markers are respectively Marker 1 at $h_1 = 0.0875m$ from the tank bottom, Marker 2 at $h_2 = 0.065m$ and Marker 3 at $h_3 = 0.04m$, see also in [28].

Three different values for the initial water depths, $H = 0.2m, 0.3m$ and $0.4m$ respectively, will be tested. The different H leads to different impact forces which cause different initial deflections of the elastic plate. The entrapped air bubble, formed after the water impacting on the vertical wall, plays an important role in the latter flow evolution, including the hydrodynamic load on the elastic structure and further its elastic response. It is worth noting that the initial water depth also leads to different thicknesses of the water layer which serves as part of the cavity boundary and therefore affects the cavity's break-up process, see more details in the following subsections.

3.2 Demonstration of the effectiveness of the phase-switch correction in the APR for multi-phase flows

In order to demonstrate the necessity and effectiveness of the correction algorithm as proposed in Section 2.1.2 when extending the adaptive particle refinement to simulations of multi-phase flows, a numerical test based on the dam-breaking flow impacts an elastic plate with the initial water depth $H = 0.2m$ is carried out in this subsection. The particle resolution adopted for the simulation is $H/\Delta x = 150$ for the initial water column. The size of the APR zone is the same as the one indicated in Figure 1.

In this test, after the water tongue hits the elastic plate, a very thin flow jet is created and is about to penetrate the multi-resolution interface (red dashed-line in Figure 3) at around $t = 0.299s$, see the first plot on the left side of Figure 3. The water jet is very thin and can only be resolved with the refined particle resolution. In other words, behind the refined water jet, there is no enough coarse and inactive water particles that are following the motions of these refined water particles.

After the jet with a finer resolution penetrates the multi-resolution interface and enters the guard zone (the zone with refined resolution outside the red dashed-line in Figure 3), the refined particles are switched into inactive particles whose variables are interpolated from the underlying active particles which are coarse. Since at this instant, the coarse particles under these refined fluid jets are all gas particles, the inactive fluid particles will inherit the velocity from the gas according to the interpolation formula (see Eq. (10)). This is the case of implementing the APR for multi-phase flows without using the phase-switch correction and the results are

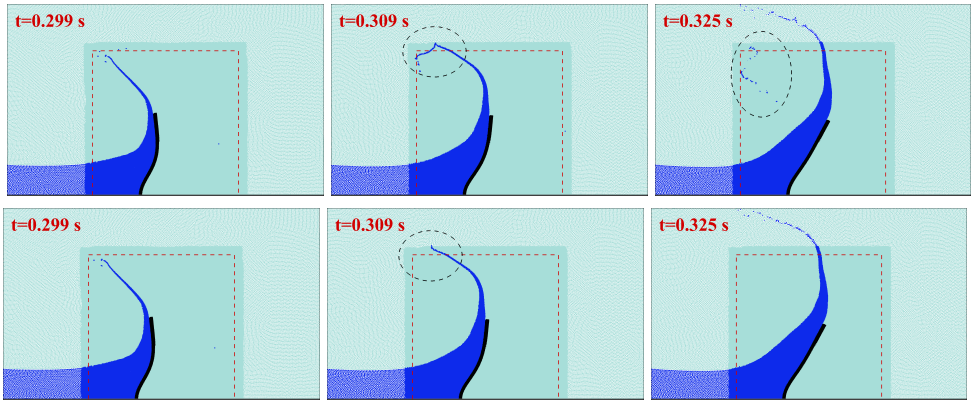

Fig. 3. Dam-breaking flow impacts an elastic plate with the initial water depth as $H = 0.2m$: comparison for the SPH results without (top panels) and with (bottom panels) the phase-switch correction (see Section 2.1.2) in the implementation of the adaptive particle refinement for multi-phase flows.

depicted on the top panels in Figure 3. One can observe that, as emphasized by the dashed elliptical circles, there are some water particles which are reflected from the multi-resolution interface with the velocity inherited from the gas particles. The reflection of the water particles is a non-physical behavior and will adversely affect the subsequent flow evolution.

On the contrary, after implementing the phase-switch correction, the result, shown on the bottom panels of Figure 3, allows a smooth penetration of the thin water jet across the multi-resolution interface. The is achieved by switching the inactive water particles in the guard zone into gas particles when they cannot inherit variables from any nearby active water particle. Therefore, this test-case clearly indicates that, for complex multi-phase simulations, the APR technique should be implemented along with the phase-switch correction to switch the inactive particles into another phase when their phase character is isolate from the surrounding active particles (i.e. all the active neighboring particles are from a different phase with respect to the considered inactive particle).

3.3 Comparison between the single-phase and multi-phase simulations

In this section, two SPH simulations are carried out, respectively considering or ignoring the air-phase, for the dam-breaking flow with the initial water depth as $H = 0.4m$. The initial condition for the SPH simulation is illustrated in Figure 1, except for the single-phase simulation where the APR zone is broadened to be $0.2m$ in the horizonal side-length since the elastic plate deflects in a larger magnitude when neglecting the air effect. The sound speed in water is determined as $c_w = 10\sqrt{2gH} = 28m/s$ according to Eq. (4) and for the multi-phase SPH simulation, the sound speed of air can be obtained with Eq.(5) as $c_a = 396m/s$ which is not far from the physical sound speed in air and therefore can give a proper estimation of

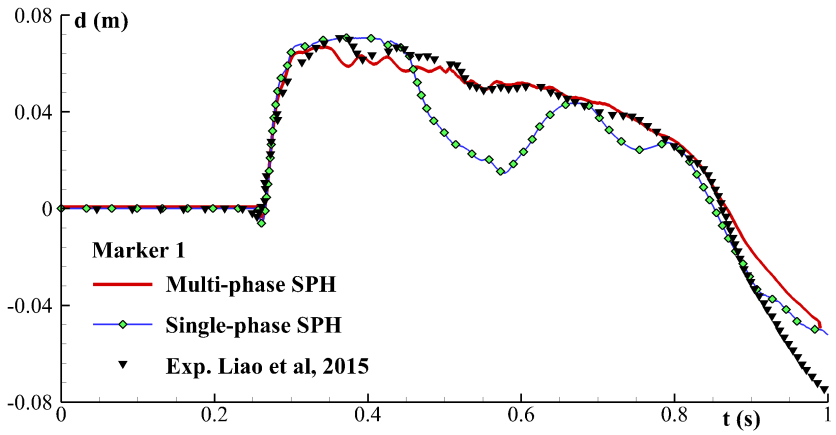

Fig. 4. Time evolutions of the horizontal displacements of the marker 1 on the elastic plate in the dam-breaking flow with an initial water depth of $H = 0.4m$: the single-phase and multi-phase SPH results are compared against the experimental data from [28].

the air compressibility. The particle resolution adopted for the two simulations are both $H/\Delta x = 300$ for the initial water column. The resolution $H/\Delta x = 300$ has been shown in [34] to be sufficiently enough for an accurate dam-breaking simulation using the δ-SPH method. When the water enters the APR zone (see Figure 1), the particle resolution is refined to $H/\Delta x = 600$ which sufficiently guarantees the local accuracy near the elastic plate where the fluid impact occurs.

Time evolutions of the horizontal displacements of the marker 1 on the elastic plate are plotted in Figure 4 where both the single-phase and multi-phase SPH results are compared against the experimental data [28]. The reverse deflection of the marker 1 on the top of the plate at $t = 0.25s$ is also captured in the SPH results. That's because the thin water front initially impacts the bottom of the plate. The strong impact force gradually bends the plate form the bottom to the top, which leads to a negative acceleration on the top of the plate. We can observe an overall agreement between the SPH results and the experimental data, however, a large discrepancy exists for the result of the single-phase SPH simulation during the duration $0.45s < t < 0.8s$. In this period, the entrapped air cavity plays an important role.

We depict the flow evolutions and the elastic plate deflections at different time instants in Figure 5 where the single-phase SPH results are compared against the multi-phase SPH results. At the initial stage of the flow impact, the two SPH models present almost identical flow features and the plate deflections. This explains the fair agreement for the plate deflections in Figure 4 when $t < 0.35s$; however, after the flow impacts the vertical tank wall on the right side, the effect of the cavity starts to be dominant. In the latter process, the back-flowing water goes along the tank bottom to the elastic plate and finally impacts again on its right side, which further affects the plate deflection and forms a big cavity surrounded by water. However, if we ignore the existence of the air phase, the vacuum cavity can be easily suppressed/expanded and therefore the second impact on the right side of the plate is much stronger, which leads to the nonphysical decrease of the displacement

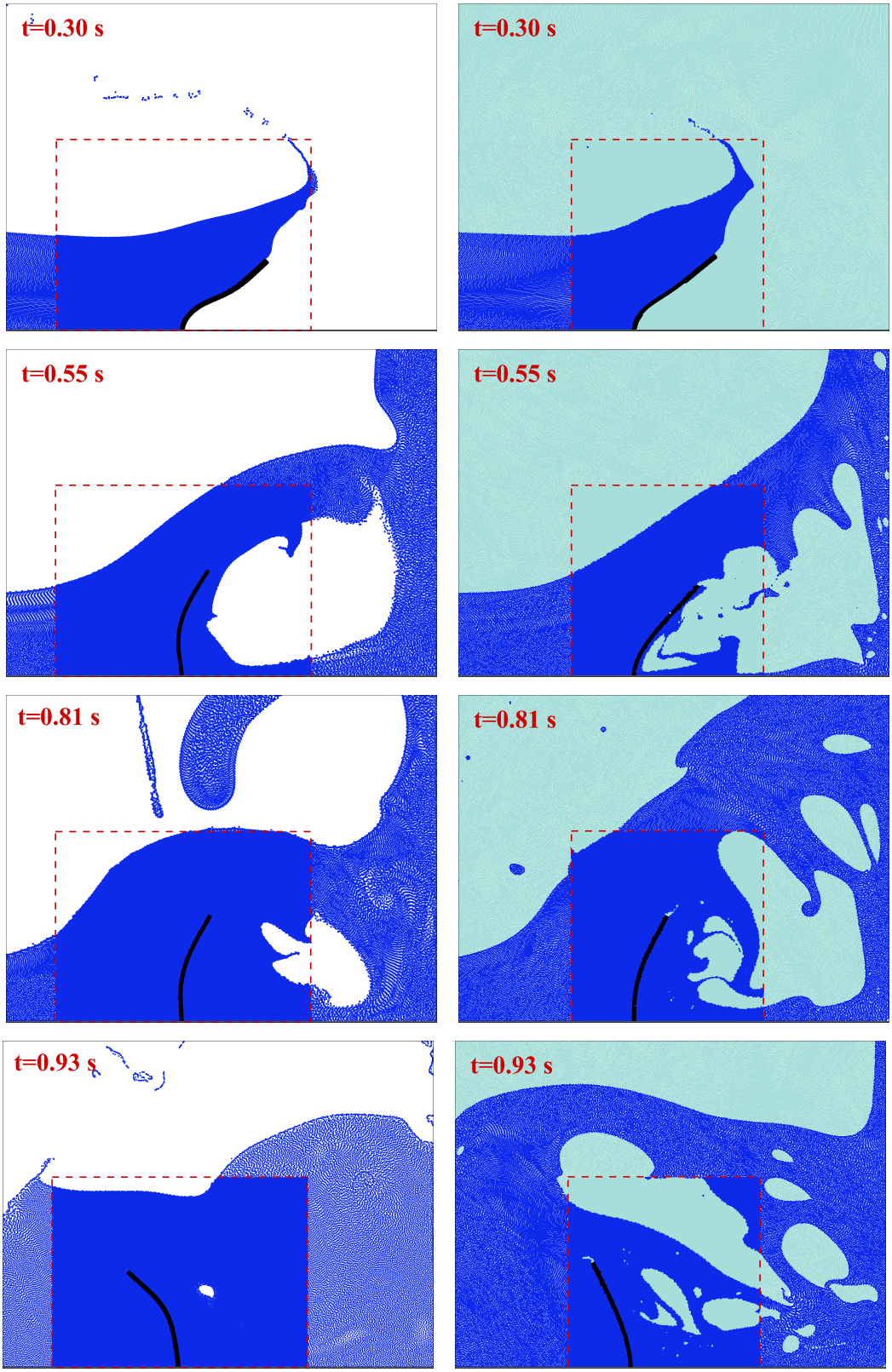

Fig. 5. Flow evolutions and the elastic plate deflections at different time instants in the dam-breaking flow with an initial water depth of $H = 0.4m$: the single-phase SPH results (left) are compared against the multi-phase SPH results (right).

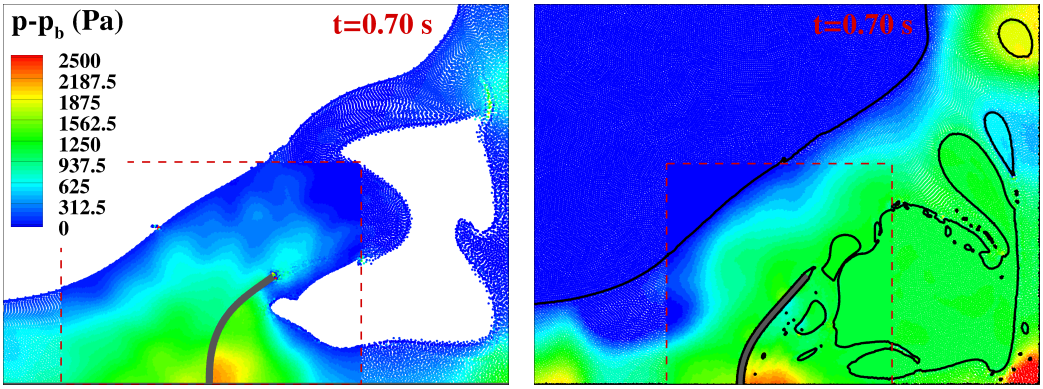

Fig. 6. The pressure field at the time instant $t = 0.7s$ in the dam-breaking flow with an initial water depth of $H = 0.4m$: the single-phase SPH result (left) is compared against the multi-phase SPH result (right).

of marker 1 in the single-phase result as plotted in Figure 4.

In the results of the multi-phase SPH in Figure 5, the total cavity volume is maintained almost constant by the existence of the air particles. The suppressing by the flow over the deflected plate leads to the pressure oscillation inside the cavity which further leads to the vibrating of the plate tip and a wavy-motion on the water-air interface(see the right plot at $t = 0.55s$), while in the single-phase simulation at the same time, since the pressure inside the cavity is zero (vacuum), the cavity volume is gradually reduced and no wavy-motion of the water-air interface is observed. From the sub-figures at $t = 0.81s$, the cavity volume of the single phase simulation has been significantly reduced while on the right side, the cavity volume still maintains but the big cavity has been split into several smaller bubbles due to the wavy-motion of the water-air interface. Finally, at $t = 0.93s$, the cavity almost disappears on the left side, which is completely different from the result of the multi-phase SPH model.

Figure 6 depicts the comparison for the pressure field in the dam-breaking problem simulated with the single-phase and multi-phase SPH method. As can be observed that in the latter case, the pressure inside the cavity is significantly larger than zero, which leads to a different flow evolution with respect to the result of the single-phase SPH model. The different phenomena of the flow evolutions and pressure fields in Figures 5 and 6 can well explain the discrepancy between the single-phase SPH result and experimental data as observed in Figure 4, which highlights the importance to consider the air-phase in such kind of complex FSI problem. Therefore, in the following sections, only multi-phase SPH simulations will be carried out for the rest of the study.

3.4 Multi-phase SPH simulations against experimental results

In this section, the multi-phase SPH model is adopted to model the series dam-breaking flow experiments as conducted by Liao et al. [28]. We divide the flow evolution into two stages, called the initial stage and the latter stage respectively, before and after the flow impacts the tank wall on the right side. The SPH simulations are conducted for three initial water depths as $H = 0.2m, 0.3m$ and $0.4m$, under which the flow evolutions are apparently different, especially in the latter stage. We carefully compare the SPH results against the experimental data as well as the other numerical solutions. With the SPH results, we analyze the mechanism behind the complex evolution of the water-air interface, showing the strong capability of the multi-phase SPH model in solving such kind of complex interfacial flows.

3.4.1 Initial depth of the water column as $H = 0.4m$

In the first subsection, the dam-breaking flow impacts an elastic plate with the initial water depth as $H = 0.4m$ is simulated and analyzed. The resolution $H/\Delta x = 300$ is adopted for the flow outside the APR zone (see Figure 1), inside which the particle resolution is refined to be $H/\Delta x = 600$.

The snapshots at 5 time instants in the initial impact stage are depicted in Figure 7 where the SPH results are compared against the experimental snapshots [28]. A good agreement is observed for the flow shape and the plate deflection. The flow front composed by the splashing droplets in the experimental snapshot is slightly larger than the one predicted by the two dimensional (2D) SPH method. This is mainly due to the dominant three dimensional (3D) effect for diffusing the splashing droplets in the experiment [28]. Similar reduced splashing phenomena are also observed from the 2D numerical results in Liao et al.[28] and Martínez-Ferrer et al. [38].

In Figure 8, we further compare the flow evolutions between the multi-phase SPH results and the experimental snapshots in the latter stage during which the cavity effect is dominant. Due to the suppression from the cavity, the amount of water flows along the tank wall is reduced and disturbed into complex droplets and therefore the strength of the second impact on the right side of the plate is weaker. Observing the experimental snapshots on the right side of Figure 8, the water-air interface is misty due to the 3D effect while on the left side, the Lagrangian nature of the SPH method allows for an exact tracking of the sharp interface, even the interface is frequently disturbed, split or reconnected by the small droplets. In addition, the wavy-motions generated by the oscillating of the plate tip on the upper part of the cavity are quite similar between the experimental snapshots and the SPH results, which has demonstrated the accuracy of the present SPH model to consider the

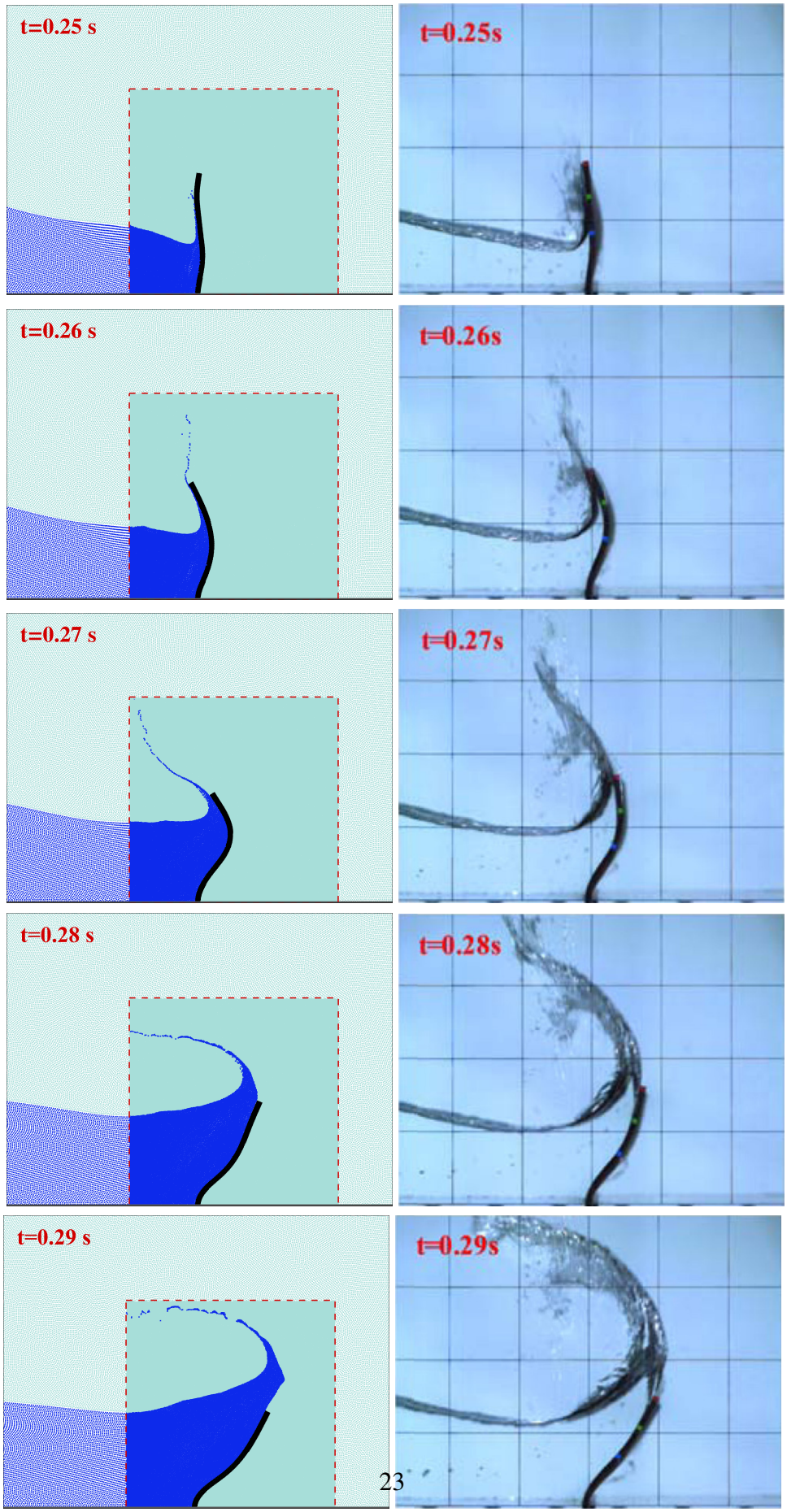

Fig. 7. Dam-breaking flow impacts an elastic plate with the initial water depth as $H = 0.4m$: the flow details at 5 time instants in the initial impact stage; the multi-phase SPH results are compared against the experimental data from Liao et al. [28].

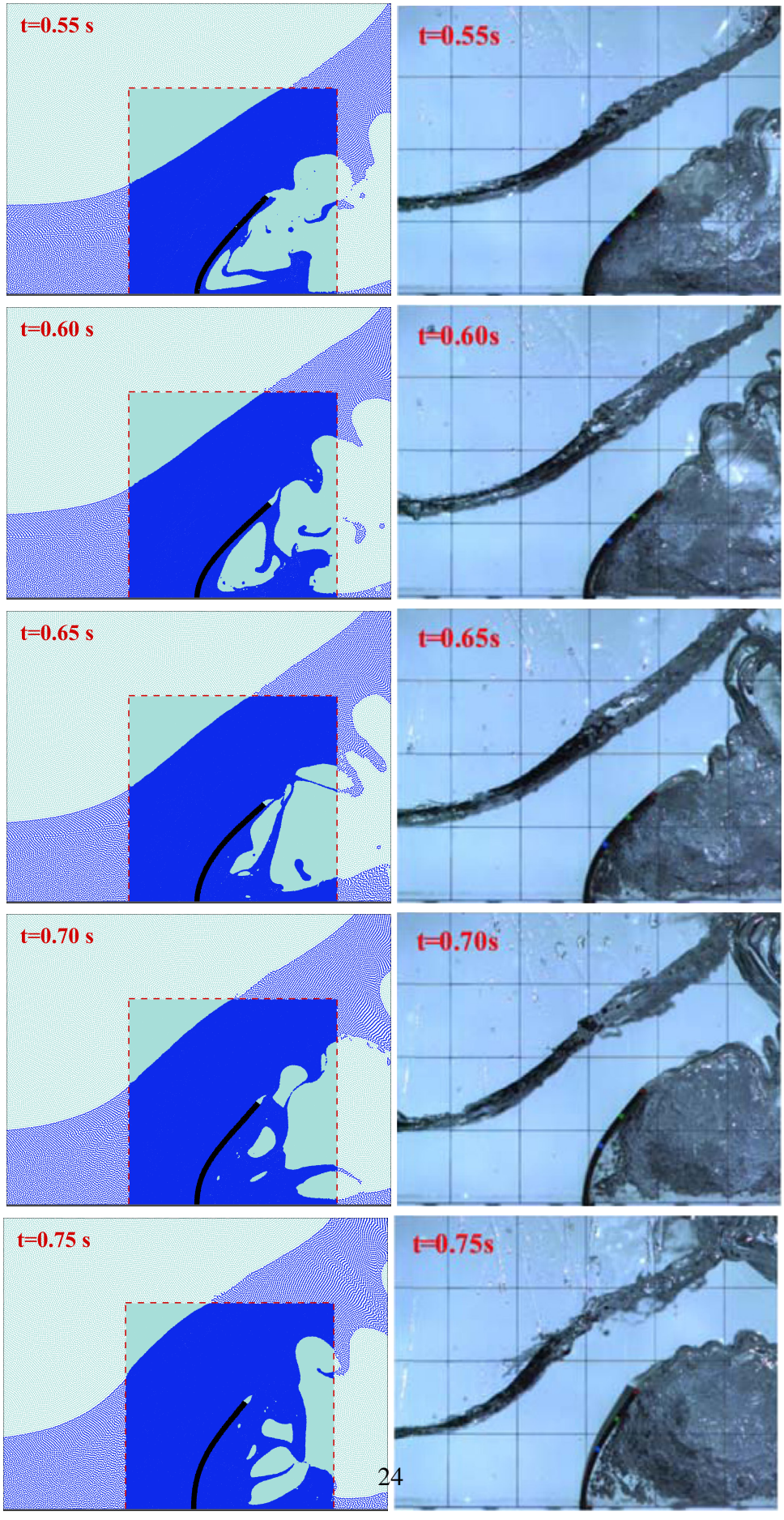

Fig. 8. Dam-breaking flow impacts an elastic plate with the initial water depth as $H = 0.4m$: the flow details at 5 time instants in the latter impact stage. The multi-phase SPH results are compared against the experimental data from Liao et al. [28].

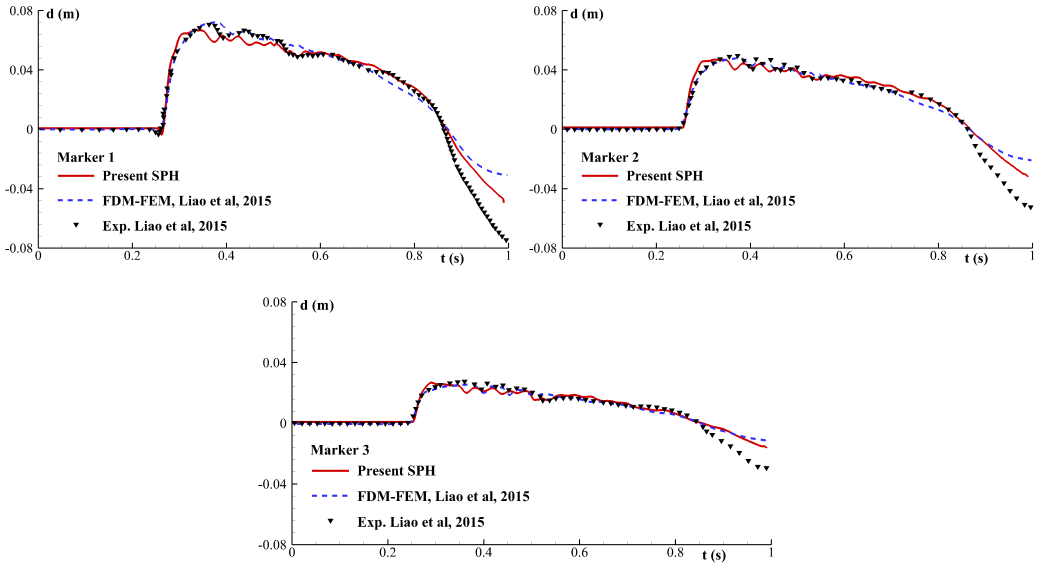

Fig. 9. Time evolutions of the horizontal displacements of the markers 1, 2 and 3 on the elastic plate in the dam-breaking flow with an initial water depth of $H = 0.4m$: the SPH results are compared against the experimental data and FDM-FEM results from Liao et al.[28].

effect of the pressure oscillation inside the cavity.

In order to present a quantitative validation for the numerical results, time evolutions of the horizontal displacements of the markers 1, 2 and 3 are plotted in Figure 9 where the SPH results are compared against both the experimental data and the numerical solution by a Finite Difference Method coupled with the Finite Element Method (FDM-FEM)[28]. A good agreement is obtained among the three solutions when $t < 0.8s$, while at the end of the dam-breaking flow, both the SPH and FDM-FEM results present slightly larger displacements than the experimental data. This can be generated by the 3D effect in the experiment where the variation in the z-direction (perpendicular to the the 2D flow plane) becomes non-negligible at the end stage of the cavity evolution.

3.4.2 Initial depth of the water column as $H = 0.3m$

In this subsection, we consider the dam-breaking flow with a lower initial water depth as $H = 0.3m$. The sound speed in water is determined as $c_w = 10\sqrt{2gH} = 24.3m/s$ according to Eq. (4) and the sound speed of air can be obtained with Eq.(5) as $c_a = 343m/s$. Similar flow evolutions will be obtained as the case in the last subsection, but here since the initial potential energy is less, the velocity and the kinetic energy of the water front when reaching the plate is smaller, and therefore the impact force and hence the plate initial deflection are reduced. Another consequence of the reduced initial water depth is in the latter stage of the flow evolution, the 3D effect is more easily to be triggered as the ratio between the water depth and tank width is reduced.

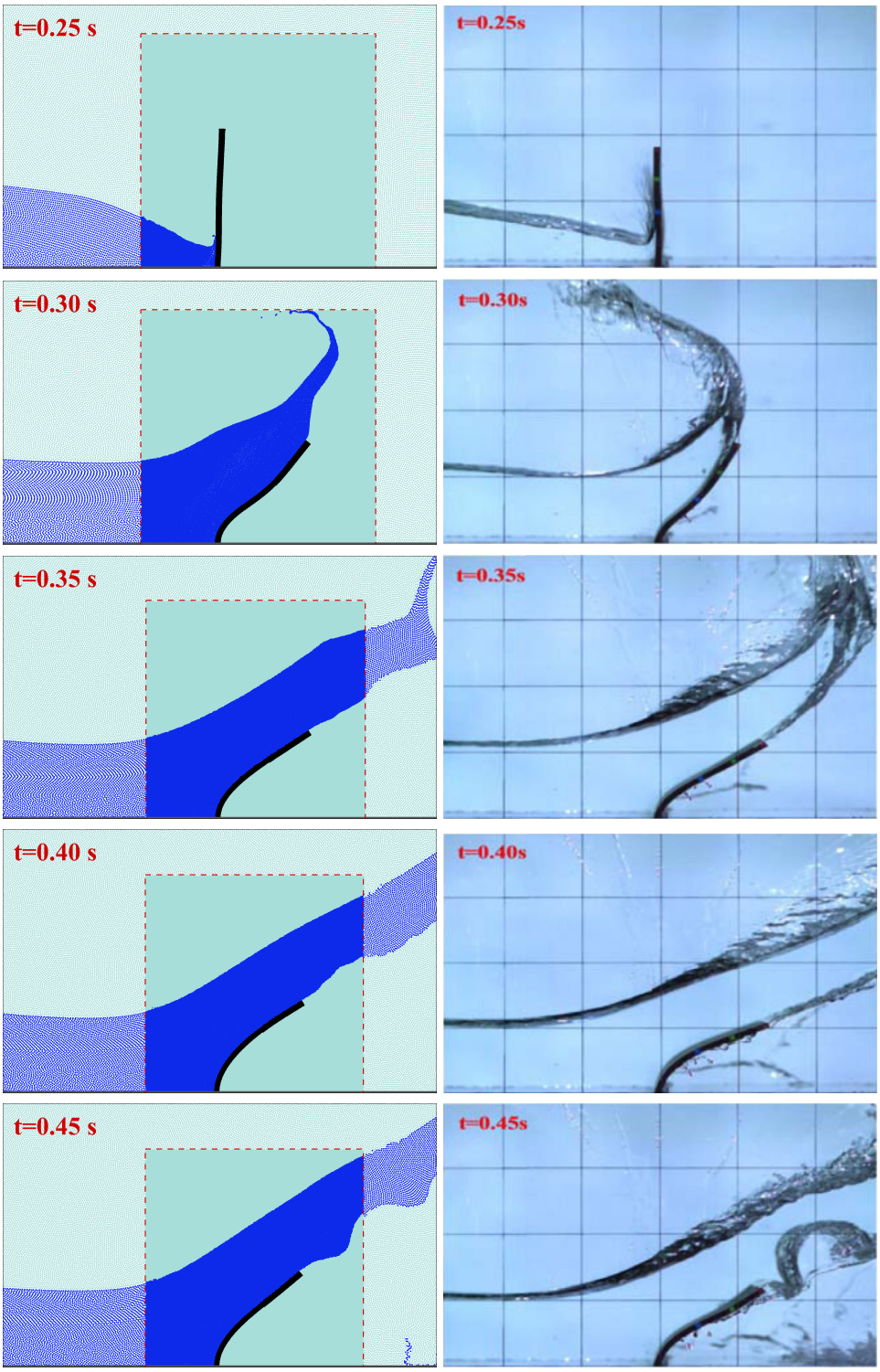

Fig. 10. Dam-breaking flow impacts an elastic plate with the initial water depth as $H = 0.3m$: the FSI-SPH results are compared against the experimental data from Liao et al. [28].

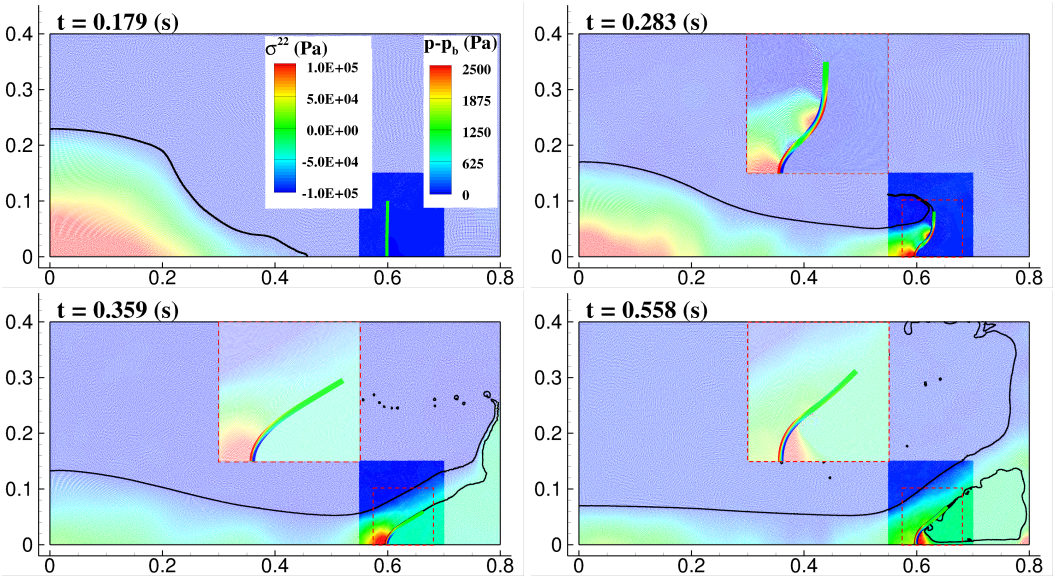

Fig. 11. Snapshots of distributions of the pressure in the fluid and enlarged portions in the red dashed box to show the stress component σ^{22} in the structure at different time instants in the dam-breaking flow with an initial water depth of $H = 0.3m$.

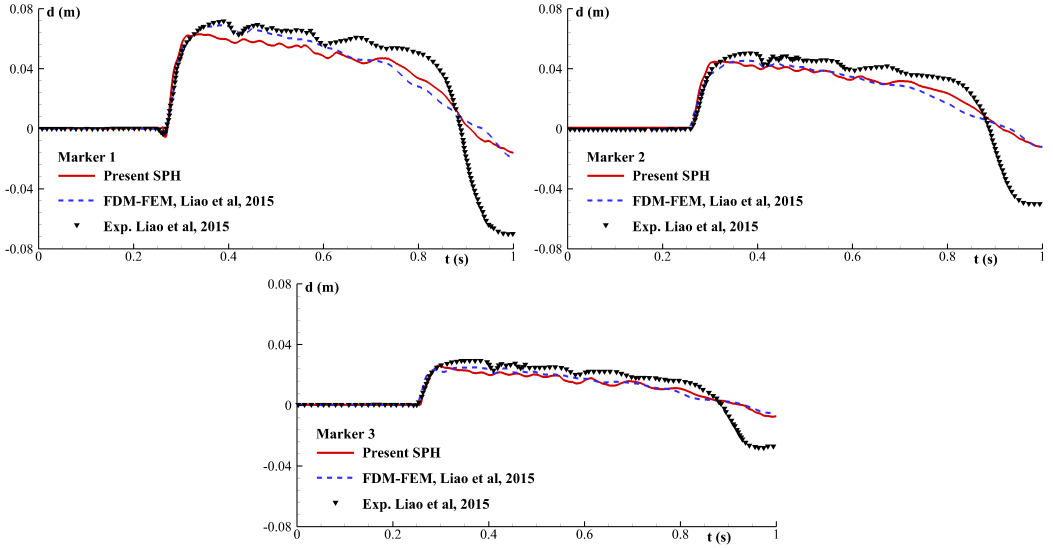

Fig. 12. Time evolutions of the horizontal displacements of the markers 1, 2 and 3 on the elastic plate in the dam-breaking flow with an initial water depth of $H = 0.3m$: the SPH results are compared against the experimental data and FDM-FEM results from [28].

Figure 10 depicts the comparison between the SPH snapshots against the experimental phenomena [28]. Good agreements are obtained at different time instants, including the disturbance of the cavity boundary due to the vibration of the elastic plate, see the time instant at $t = 0.45s$.

Snapshots of distributions of the pressure in the fluid and enlarged portions to show the stress component σ^{22} in the structure at different time instants are depicted in Figure 11. Thanks to the δ-term added in the continuum equation, the pressure

field is resolved without noise. The background pressure above the free surface is maintained to be stable around the background pressure p_b. We underlined that, after the flow impacts the vertical wall on the right side, the pressure inside the cavity increases due to the continuous suppression from the water. The pressure fluctuation inside the cavity is a dominant factor which affects the response of the elastic plate.

For a quantitative validation, time evolutions of the horizontal displacements of the markers 1, 2 and 3 on the elastic plate are plotted in Figure 12. We find that the overall agreement between the numerical results and the experimental data are only valid at the initial impact stage, after $t = 0.8s$, the discrepancy is larger. As communicated with the authors of the experiment [28], the increasing 3D phenomenon was observed at the final stage of the experiment. This explains why the two numerical solvers in 2D (SPH and FDM-FEM) give practically identical results, but both of them slightly diverge from the experimental data.

3.4.3 Initial depth of the water column as $H = 0.2m$

In this subsection, we further reduce the initial water depth to be $H = 0.2m$. The sound speed in water is determined as $c_w = 10\sqrt{2gH} = 19.8m/s$ according to Eq. (4) and the sound speed of air can be obtained with Eq.(5) as $c_a = 280m/s$. In this case, the thickness of the water layer after impacting the elastic plate is very thin; therefore, the entrapped cavity is easily to break up. Figure 13 depicts the flow evolutions after the water front impacts the plate. The SPH snapshots on the left of the figure are validated by the experimental snapshots on the middle [28] and the numerical solution by Martínez-Ferrer et al.[38] on the right side.

After the water jet impacts the vertical tank wall on the right side, the cavity is formed and the pressure pulsation inside the bubble leads to the oscillation of the elastic plate which further causes disturbances on the water-gas interface on the top of the air bubble, see the comparison of the SPH snapshots and the experimental results [28] in Figure 14. Since here the water layer above the bubble is much thinner with respect to the previous cases with larger initial depths, the disturbance is enlarged at $t = 0.58s$ and the bubble almost breaks up at $t = 0.69s$. During this stage, the SPH results agree well with the experimental observations thanks to the exact capturing of the water-gas interface by the Lagrangian particle method. To our knowledge, the numerical results for this test-case at this stage (cavity formation and breakup) were not reported by using the other mesh-based numerical solvers. Observing the snapshot at $t = 0.69s$, after the breakup of the cavity, a new water block is formed and will create the second impact (see also the experimental result in Liao et al. [28]) on the elastic plate. After the completeness of the second impact, two air bubbles are formed when the new water front connects the underlying water surface on the right side, see the snapshots on the left side of Figure 15. After that, the increasing pressure inside the new formed bubble pushes the plate to the left

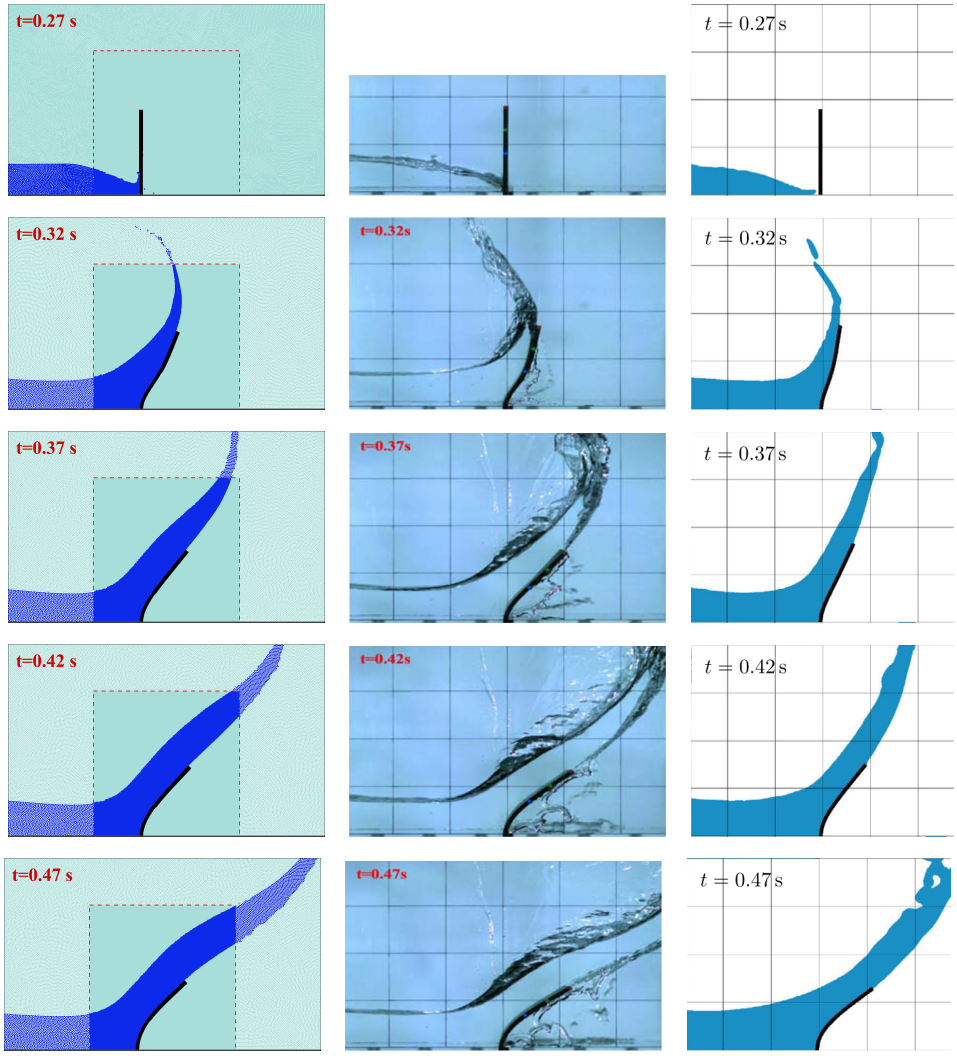

Fig. 13. Dam breaking flow impacts an elastic plate: the flow details at 5 time instants. The FSI-SPH results are compared against the experimental data from Liao et al. [28] and the numerical solution by Martínez-Ferrer et al. [38].

side and therefore leads to the rebound of the elastic plate to its initial position, see on the right side of Figure 15.

We measured the time evolutions of the horizontal displacements of the markers 1, 2 and 3 on the elastic plate and the curves are plotted in Figure 16, comparing against the experimental data [28]. One can observe that the overall trend of the SPH results agree better with the experimental data than the numerical results reported in [28]. The SPH results better capture the first and second impacts on the plate thanks to the more accurate capturing of the complex water-air interface. The two impacts were only analyzed by the experimental data in [28] while the numerical solutions by the mesh-based CFD solvers were not shown. The initial deflection of plate in the SPH results are slightly smaller than the experimental data. The reason will be analyzed in the next subsection. However, the present SPH results during the final stage of this test agree better with the experimental data than Liao's FDM-FEM

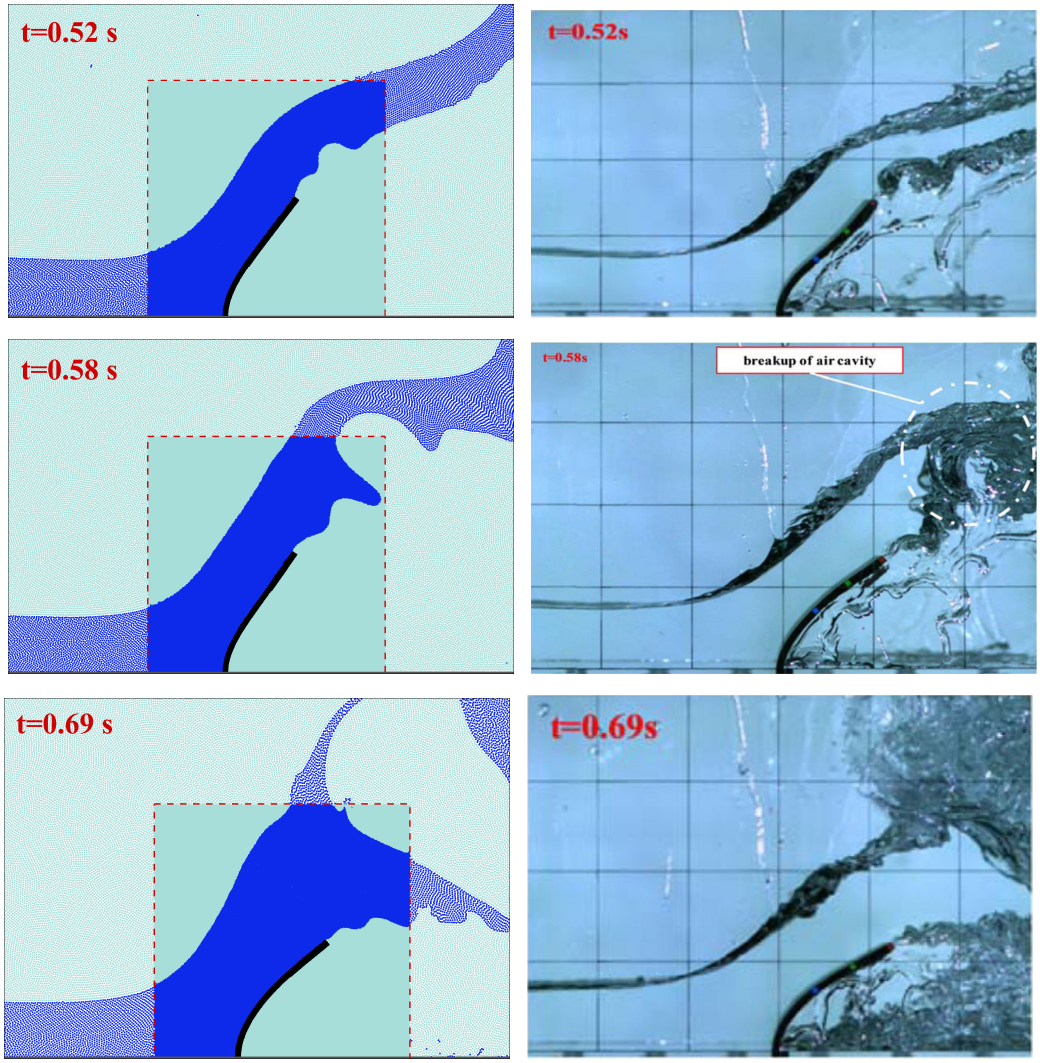

Fig. 14. Dam breaking flow impacts an elastic plate: the flow details at 3 time instants after the formation of the cavity. The FSI-SPH results are compared against the experimental snapshots from Liao et al. [28].

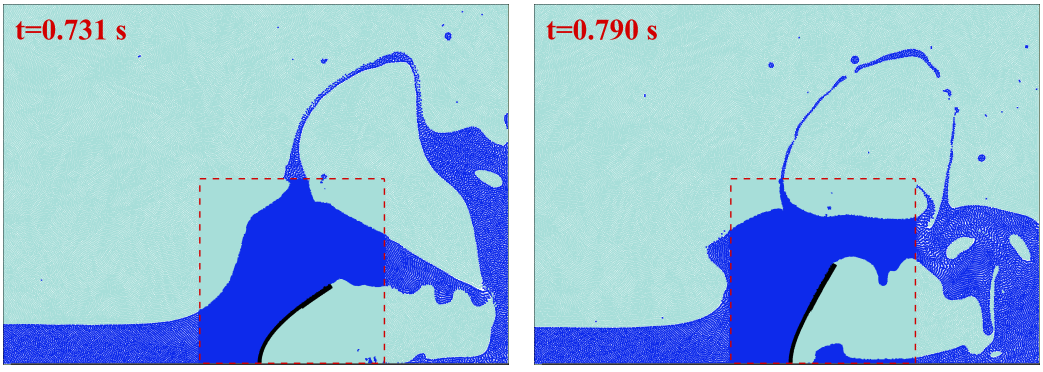

Fig. 15. Dam breaking flow impacts an elastic plate: the flow details at 2 time instants during which the previous cavity is divided into two parts, the one on the top breaks up and the one on the bottom leads to the rebound of the plate to the vertical position.

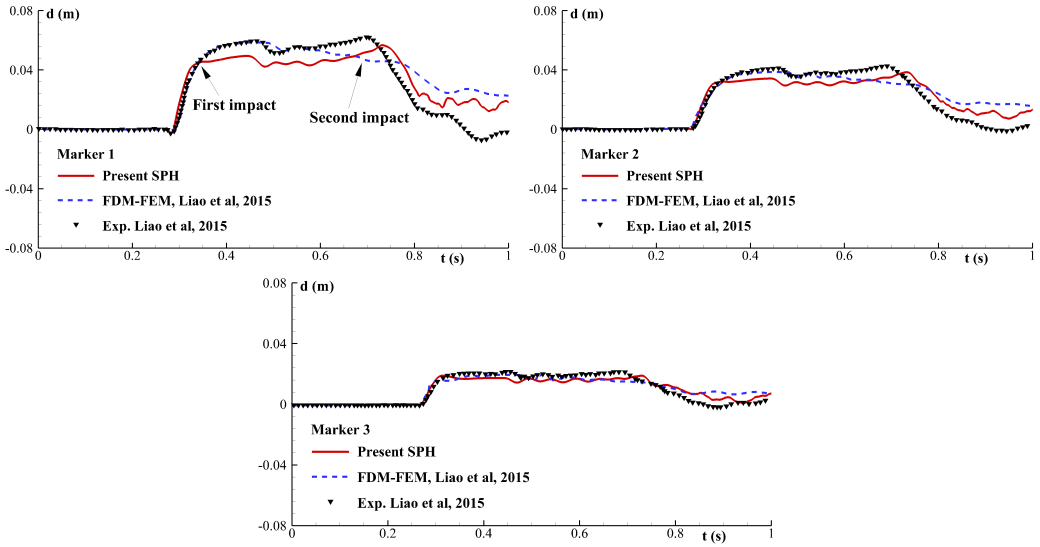

Fig. 16. Time evolutions of the horizontal displacements of the markers 1, 2 and 3 on the elastic plate in the dam-breaking flow with an initial water depth of $H = 0.2m$: the SPH results are compared against the experimental data and FDM-FEM results from Liao et al. [28].

solutions [28].

3.5 Discussions on the plate deflection at the initial impact stage

3.5.1 Effects of the particle resolutions

In the previous section, the dam-breaking flows impacting the elastic plate have been modeled by the multi-phase δ-SPH model coupled with a TLP method and the numerical results are compared against the experimental results [28]. The cavity effect on the latter stage of the flow impact has been emphasized. However, besides the overall agreement between our numerical solutions and the experimental data, for the cases with the shallower initial water depths (i.e. $H = 0.3m$ and $H = 0.2m$), slight discrepancies for the plate deflection at the initial impact stage are observed. Therefore, in this subsection, we firstly carry out a numerical study to test the effect of the particle resolution, despite the fact that a sufficient particle resolution has been adopted in the last section comparing with the dam-breaking flow simulations in Marrone et al. [34].

Here we run two dam-breaking test-cases of $H = 0.3m$ and $H = 0.2m$ with the particle resolution as $\Delta x = 5.0 \times 10^{-4} m$ inside the APR zone to see the difference of the initial plate deflection. The results are reported in Figure 17, comparing against the results with $\Delta x = 6.67 \times 10^{-5} m$ which is used in the previous subsection. Finally, we find that the SPH results with the two particle resolutions are practically identical, which confirms that the previous SPH results are not affected by refining the particle resolutions.

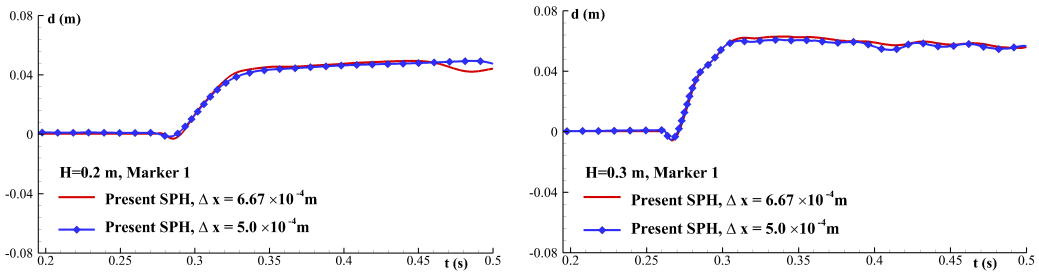

Fig. 17. Time evolutions of the horizontal displacements of the marker 1 at the initial impact stage in the dam-breaking flows with the initial water depths as $H = 0.2m$ (left panel) and $H = 0.3m$ (right panel): results of different particle resolutions are compared.

3.5.2 Comparisons between different 2D multi-phase solvers

After the exclusion of the effect of the particle resolution as investigated in the previous subsection, in this subsection we present a short discussion for explaining why the 2D SPH results of the initial plate defections in the dam-breaking cases with $H \leq 0.3m$ is slightly smaller than the experimental data.

Firstly, in order to demonstrate the fact that the discrepancy between the numerical and experimental data is not generated by the SPH method itself, we compare the SPH results against some other published numerical solutions (the FDM-FEM results from [27] and the FVM-FEM solution from Martínez-Ferrer et al. [38]) in Figure 18 where the deflections on Marker 1 during $t < 0.5s$ under three different initial water depths are plotted. The three numerical solutions present fair agreements for the cases of $H = 0.4m$ and $H = 0.3m$, while in the last subplot, the FVM-FEM solution presents a slower increase of the deflection, however the average value is still similar to the present SPH solution and the FDM-FEM solution in [27]. The disagreement of the solution in Martínez-Ferrer et al.[38] with respect to the present SPH solution can be attributed to the ignorance of the gate motion as stated in [38].

Since the present SPH solutions obtained under the weakly compressible hypothesis have shown agreement with the incompressible results in the literature [38], see Figure 18. We can eliminate the effect from the artificial compressibility of water during the initial impact stage. Indeed, it has also been proven in Marrone et al. [37, 35] that within the weakly-compressible regime the Mach number effect is limited for water impact problems. In addition, in the initial impact stage, since the air cavity is still not formed, the effect of the air phase is not dominant.

As can be found in Section 3.4.1, the initial deflection of the plate predicted by the 2D numerical method for $H = 0.4m$ agrees well with the experimental data, while when H reduces to $0.3m$ in Section 3.4.2, a slight discrepancy is observed for the maximum deflection on Marker 1. Fortunately, for that case the discrepancy reduces on Marker 2 and 3. However, in the last test of $H = 0.2m$, see Section 3.4.3, the discrepancy at the initial stage is the most distinct. We summary two possible

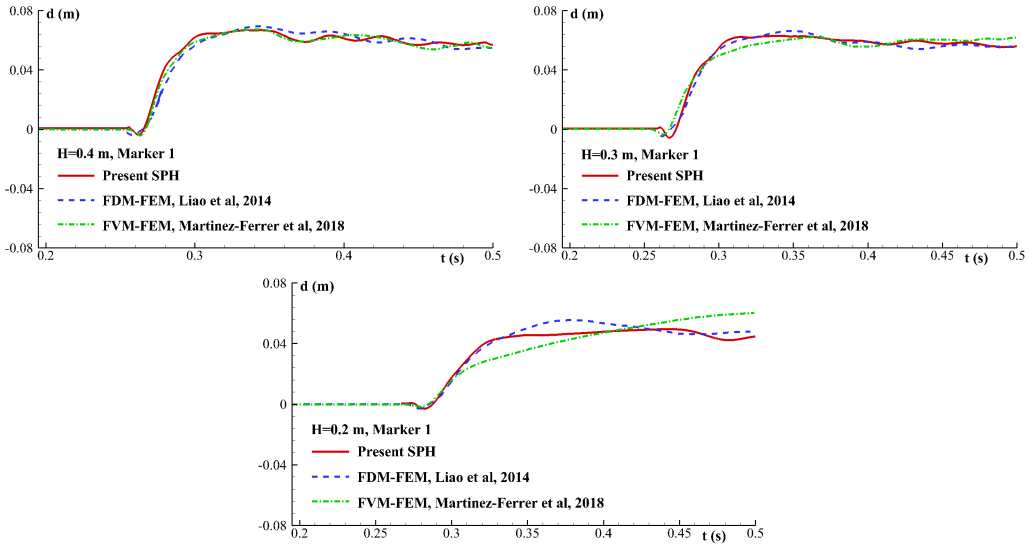

Fig. 18. Time evolutions of the initial horizontal displacements of the marker 1 on the elastic plate in the three dam-breaking flows with the initial water depths as $H = 0.4m, 0.3m$ and $0.2m$ respectively: the SPH results are compared against the corresponding FDM-FEM results from [27] and the FVM-FEM solution from Martínez-Ferrer et al.[38].

reasons which can lead to these discrepancies:

- The 3D effect in the experiment has not been considered in the 2D simulation. This can be justified by the fact that when the ratio H/W between the initial water depth H and the width of the tank ($W = 0.2m$ in the experiment [28]) is enlarged, the discrepancy is smaller since the 3D effect is reduced as the increase of H/D;
- The nonlinearity of the elasticity modulus for the plate has not been considered in the numerical simulation. As has been highlighted in Li et al. [26] that the numerical results converge to the experimental data only when a nonlinear elasticity model is applied. A constant elastic modulus can over predict the stress as the deformation becomes larger and therefore reduce the plate defection. On the other hand, when the water depth is larger, the fluid force is dominant, under which the effect of the nonlinear elasticity is not apparent, however, in the shallower water depth, the plate deformation is more relied on its inner stress. Therefore, for the last two cases studied before, the nonlinearity of the plate needs to be considered. However, the data for the tensile test of the elastic plate was not reported in the literature [28] and therefore only a linear model is adopted in the present SPH simulation, which is the same case in the simulations of [27] and [38].

4 Conclusions and future works

In the present work, the δ-SPH scheme has been further extended to the multi-phase FSI context and complex interactions between the water, air and the elastic structure are modeled, validated and analyzed. Thanks to the Lagrangian and mesh-less characters of the adopted method, the multi-phase SPH scheme has been shown to be able to accurately capture the multi-phase and fluid-structure interfaces and well resolve the interactions between them, regardless of the magnitudes of these deformations.

In terms of numerical method, in the present particle method, the adaptive particle refinement has been extended to multi-phase flows with a phase-switch correction to ensure the accuracy and stability at the multi-phase interface. A background pressure defined according to the characteristic velocity of the flow is implemented in the SPH scheme to regularize the particle distribution, especially for the gas particle with smaller mass. The mechanism of the background pressure for adjusting the particle positions is similar to the particle shifting technique, but the latter is not mature in multi-phase weakly-compressible particle models, especially when the interface evolution is quite complex. As the magnitude of the background pressure defined in this work is not very large, in order to prevent excessive numerical dissipation, negative pressures are allowed to exist in some flow regions where, fortunately, the triggering of the tensile-instability has been completely prevented by the implementation of the TIC technique. Indeed, in the future studies, through the extension of the recently developed consistent PST [46] into the multi-phase flow and implementing the optimized treatment of PST [23] near the multi-phase interface, the background pressure and the associated unfavorable effects are hopefully to be eliminated.

In terms of numerical results, test cases of the dam-breaking flows impacting an elastic plate have been modeled to validate the particle method. Firstly, comparative test-cases with or without considering the air particles are carried out to demonstrate the importance of taking into account the air phase in such complex FSI problems. The numerical result shows that the air-bubble entrapped after the free-surface closing is dominant for the subsequent flow evolution and hence the load on the structure. After the first comparative study, the multi-phase SPH model has been adopted for a detailed study of the impact phenomena of the dam-breaking flow on the elastic plate with three different initial water depths, for which the flow and cavity evolutions are different. Good agreements of the water flow, the plate deflection and the cavity formation and collapsing are obtained between the experimental data and the numerical results. We carefully analyzed the flow features in different stages of the test-cases, providing a detailed reference for the readers who would adopt these test-cases to validate their own numerical schemes.

However, there are still some discrepancies between experimental data and numer-

ical results for the initial plate deflection and the final cavity evolution in the cases with smaller initial water depths. In those cases, the splashing fluid layer is thinner and therefore 3D flow features are easily triggered. In addition to 3D effects in the experiment, we also attribute the reason for the discrepancies to the non-linearity of the plate's elasticity modulus which was not reported in the experimental literature and hence cannot be considered in this work. Therefore, further investigations are still necessary in the future work for a 3D study with the non-linear elasticity modulus considered for the plate.

Acknowledgements

The author PengNan Sun was funded by a post-doctoral research grant from Ecole Centrale Nantes.

Appendices

A Dynamic response of an oscillating plate

In this section, based on the benchmark proposed by Turek and Hron [52], the accuracy of the TLP method is validated with the simulation of the dynamic response of an oscillating plate in the gravity field. In this test, the structure is characterized by a circular cylinder with a horizontal plate as depicted in Figure A.1 where the cylinder part is considered to be rigid and the horizontal plate is elastic. The radius of the cylinder is $R = 0.05m$. The length and thickness of the elastic plate are $L = 0.35m$ and $H = 0.02m$ respectively. The density of the plate is $\rho_0^s = 1000kg/m^3$. The Yang's modulus and Poisson's ratio are $E_s = 1.4 \times 10^6 Pa$ and $\nu_s = 0.4$, respectively. The elastic plate is released from the horizontal position at $t = 0$, after that it starts to oscillate in the gravity field of $g = 2m/s^2$. In this benchmark, the displacement at point A, which is located on the tip of the plate (see Figure A.1), is measured and compared against the reference solution provided by Turek and Hron [52] using FEM.

Firstly, we run a simulation in the TLP method with the particle resolution as $D/\Delta x = 100$ where D is the cylinder diameter. Figure A.2 depicts the elastic deformations of the plate and the distributions of the stress component σ_{11} at 4 time instants. At $t/T = 0$ (T is the oscillating period), the elastic plate is located at the horizontal position, from which it is gradually bent under the gravity force and reaches the lowest position at $t/T = 0.5$. After this time instant, it starts to rebound and recover to the horizontal state. One can find from Figure A.2 that, at

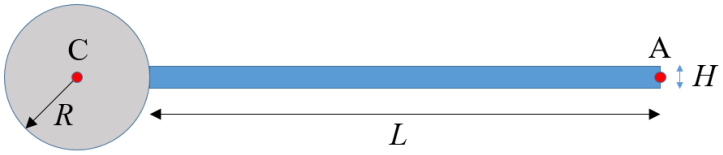

Fig. A.1. Sketch for the benchmark test proposed by Turek and Hron [52] for validating the structure solver.

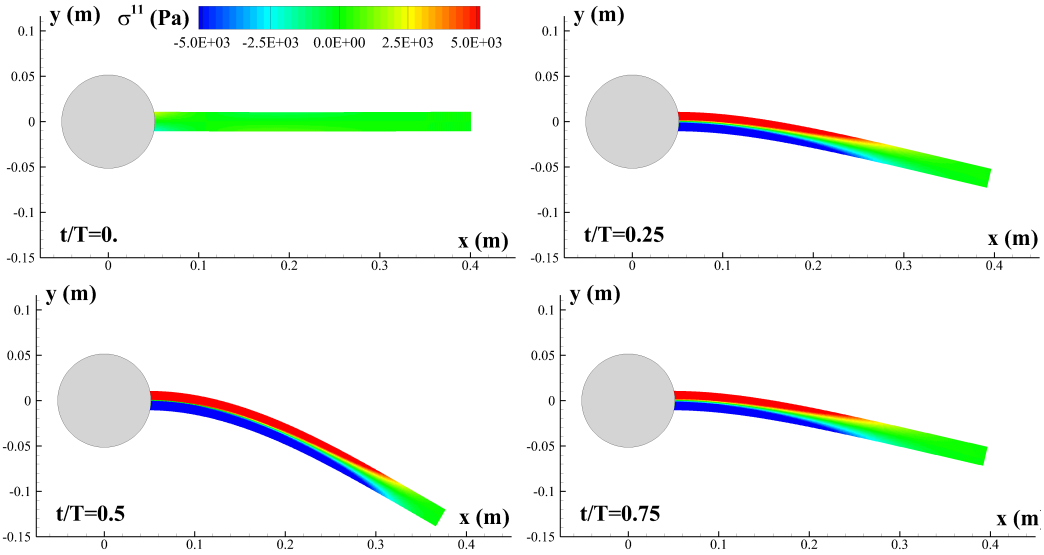

Fig. A.2. The deformations of the elastic plate and the distributions of the stress component σ^{11} at 4 time instants in one oscillating period.

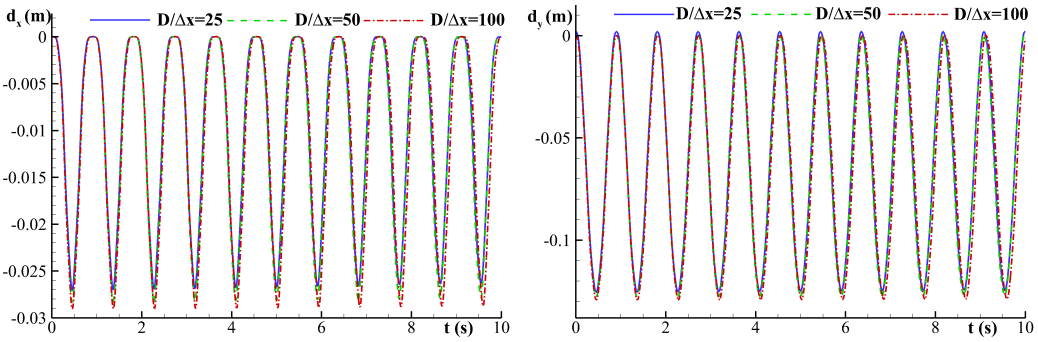

Fig. A.3. Time evolutions for the horizontal (left) and vertical (right) displacements of the point A under three different particle resolutions.

$t/T = 0.25$ and $t/T = 0.75$, the positions of the elastic plate and the stress distributions are almost identical. Further, since the Lagrangian kernel has been adopted, tensile instability is completely prevented in the region characterized by tensile stress.

In order to quantitatively validate the TLP result, Figure A.3 plots the time evolutions of the horizontal (d_x) and vertical (d_y) displacements at point A for three different particle resolutions (respectively, $D/\Delta x = 25$, $D/\Delta x = 50$ and $D/\Delta x = 100$).

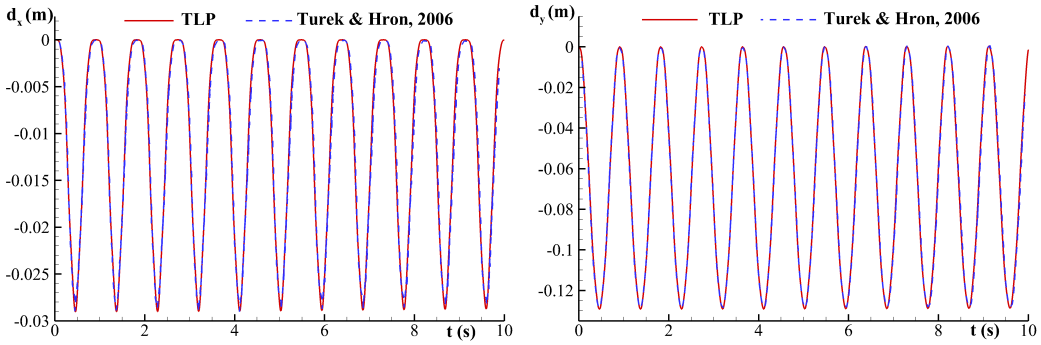

Fig. A.4. Comparison between the results of TLP and Turek and Hron [52] for the horizontal (left) and vertical (right) displacements of the point A.

As the increase of the particle resolution, one can clearly observe the convergence of the TLP solution.

Figure A.4 compares the TLP result of $D/\Delta x = 100$ against the reference solution of FEM [52] and a good agreement is obtained. The numerical results of TLP have demonstrated sufficient accuracy and therefore this structural solver can be further implemented in the FSI simulations.

B Hydrostatic water column on an elastic plate

The simulation of the hydrostatic water on an elastic plate as carried out in [22, 14, 26] is tested using the present FSI-SPH model to assess its property of stability-preserving. In this test, a water column with the height of $2m$ and width of $0.5m$ is suddenly placed on an aluminum plate with the thickness of $h_e = 0.05m$, density of $\rho_0^s = 2700kg/m^3$, Young's modulus of $E_s = 67.5GPa$ and Poisson's ratio of $\nu_s = 0.34$. The gravity acceleration is $g = 9.81m/s^2$. According to the analytical solution as provided in [14], the magnitude of the static deflection at the mid-span of the plate is -6.85E-05 m.

Two particle resolutions, respectively $h_e/\Delta x = 6$ and $h_e/\Delta x = 12$ are adopted in the present simulation. The pressure field in the fluid and the field of the stress component σ^{11} in the structure at $t = 0.1s$ with the finer resolution is depicted in Figure B.1. Further, in Figure B.2, time histories of the deflections at the mid-span of the elastic plate solved by two particle resolutions are plotted. After a transitional stage, the present SPH result with the finer particle resolution shows a good agreement with the analytical solution [14]. The numerical results presented in Figures B.1 and B.2 indicate that an accurate and steady state can be reached in this hydrostatic test, which verifies the accuracy and stability of the present FSI-SPH model.

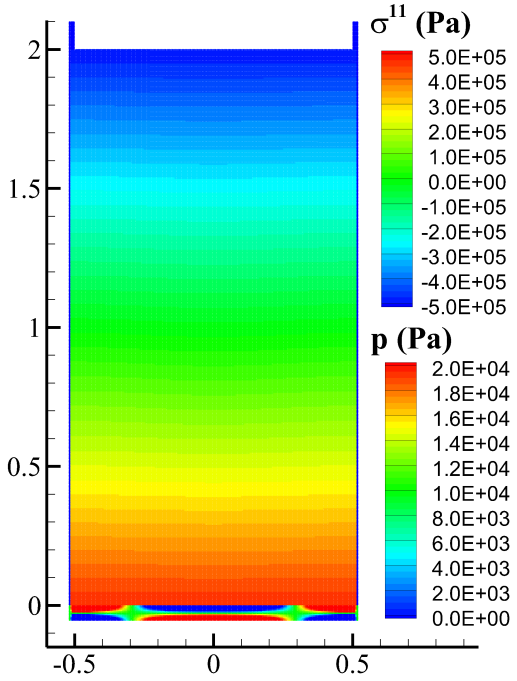

Fig. B.1. The pressure field in the fluid and the field of the stress component σ^{11} in the structure at $t = 0.1s$.

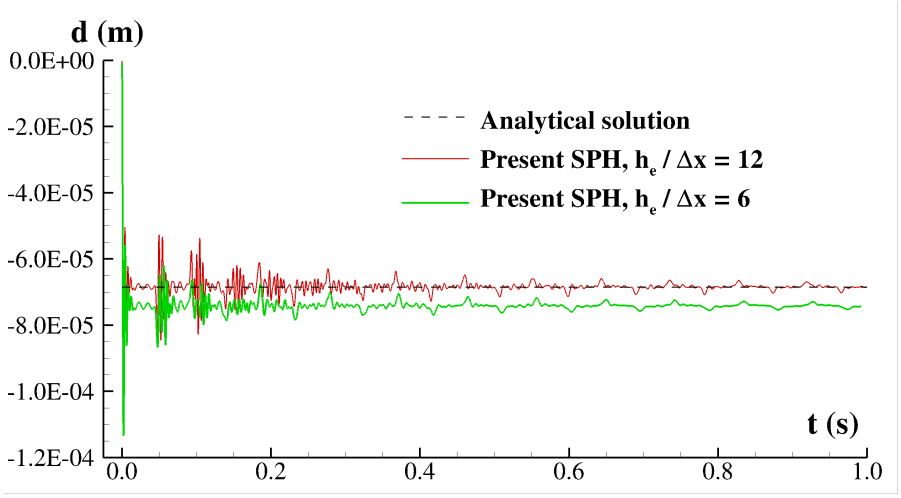

Fig. B.2. Time histories of the deflection d at the mid-span of the elastic plate under a hydrostatic water column; the FSI-SPH results with two particle resolutions are compared against the analytical solution [14].

References

[1] Adami, S., Hu, X., Adams, N.A., 2012. A generalized wall boundary condition for smoothed particle hydrodynamics. Journal of Computational Physics 231, 7057–7075.

[2] Adami, S., Hu, X., Adams, N.A., 2013. A transport-velocity formulation for smoothed particle hydrodynamics. Journal of Computational Physics 241, 292–307.

[3] Antoci, C., Gallati, M., Sibilla, S., 2007. Numerical simulation of fluid-structure interaction by SPH. Computers & Structures 85, 879–890.

[4] Antuono, M., Colagrossi, A., Marrone, S., Lugni, C., 2011. Propagation of gravity waves through an SPH scheme with numerical diffusive terms. Computer Physics Communications 182, 866–877.

[5] Antuono, M., Colagrossi, A., Marrone, S., Molteni, D., 2010. Free-surface flows solved by means of SPH schemes with numerical diffusive terms. Computer Physics Communications 181, 532–549.

[6] Barcarolo, D., Touzé, D.L., Oger, G., de Vuyst, F., 2014. Adaptive particle refinement and derefinement applied to the smoothed particle hydrodynamics method. Journal of Computational Physics 273, 640–657.

[7] Bouscasse, B., Colagrossi, A., Marrone, S., Antuono, M., 2013. Nonlinear water wave interaction with floating bodies in SPH. Journal of Fluids and Structures 42, 112–129.

[8] Chiron, L., Oger, G., De Leffe, M., Le Touzé, D., 2018. Analysis and improvements of Adaptive Particle Refinement (APR) through CPU time, accuracy and robustness considerations. Journal of Computational Physics 354, 552–575.

[9] Colagrossi, A., Antuono, M., Le Touzé, D., 2009. Theoretical considerations on the free-surface role in the Smoothed-particle-hydrodynamics model. Physical Review E 79, 056701.

[10] Colagrossi, A., Bouscasse, B., Antuono, M., Marrone, S., 2012. Particle packing algorithm for SPH schemes. Computer Physics Communications 183, 1641–1683.

[11] Colagrossi, A., Landrini, M., 2003. Numerical Simulation of Interfacial Flows by Smoothed Particle Hydrodynamics. Journal of Computational Physics 191, 448–475.

[12] Crespo, A., Dominguez, J., Rogers, B., Gomez-Gesteira, M., Longshaw, S., Canelas, R., Vacondio, R., Barreiro, A., Garcia-Feal, O., 2015. DualSPHysics: Open-source parallel CFD solver based on Smoothed Particle Hydrodynamics (SPH). Computer Physics Communications 187, 204–216.

[13] Falahaty, H., Khayyer, A., Gotoh, H., 2018. Enhanced particle method with stress point integration for simulation of incompressible fluid-nonlinear elastic structure interaction. Journal of Fluids and Structures 81, 325–360.

[14] Fourey, G., Hermange, C., Le Touzé, D., Oger, G., 2017. An efficient FSI coupling strategy between smoothed particle hydrodynamics and finite element methods. Computer Physics Communications 217, 66–81.

[15] Gotoh, H., Khayyer, A., 2018. On the state-of-the-art of particle methods for coastal and ocean engineering. Coastal Engineering Journal 60, 79–103.

[16] Grenier, N., Antuono, M., Colagrossi, A., Touzé, D.L., Alessandrini, B., 2009. An Hamiltonian interface SPH formulation for multi-fluid and free surface flows. Journal of Computational Physics 228, 8380–8393.

[17] Grenier, N., Touzé, D.L., Colagrossi, A., Antuono, M., Colicchio, G., 2013. Viscous bubbly flows simulation with an interface SPH model. Ocean Engineering 69, 88–102.

[18] Han, L., Hu, X., 2018. SPH modeling of fluid-structure interaction. Journal of Hydrodynamics 30, 62–69.

[19] Khayyer, A., Gotoh, H., 2013. Enhancement of performance and stability of MPS mesh-free particle method for multiphase flows characterized by high density ratios. Journal of Computational Physics 242, 211–233.

[20] Khayyer, A., Gotoh, H., 2015. A multi-phase compressible-incompressible particle method for water slamming, in: The Twenty-fifth International Ocean and Polar Engineering Conference, International Society of Offshore and Polar Engineers. pp. 1235–1240.

[21] Khayyer, A., Gotoh, H., 2018. Advanced Fully-Lagrangian mesh-free computational methods for hydroelastic fluid-structure interactions in ocean engineering, in: The Thirteenth ISOPE Pacific/Asia Offshore Mechanics Symposium, International Society of Offshore and Polar Engineers.

[22] Khayyer, A., Gotoh, H., Falahaty, H., Shimizu, Y., 2018. An enhanced ISPH-SPH coupled method for simulation of incompressible fluid-elastic structure interactions. Computer Physics Communications 232, 139–164.

[23] Khayyer, A., Gotoh, H., Shimizu, Y., 2019a. A projection-based particle method with optimized particle shifting for multiphase flows with large density ratios and discontinuous density fields. Computers & Fluids 179, 356–371.

[24] Khayyer, A., Gotoh, H., Shimizu, Y., Gotoh, K., 2017. On enhancement of energy conservation properties of projection-based particle methods. European Journal of Mechanics-B/Fluids 66, 20–37.

[25] Khayyer, A., Tsuruta, N., Shimizu, Y., Gotoh, H., 2019b. Multi-resolution MPS for incompressible fluid-elastic structure interactions in ocean engineering. Applied Ocean Research 82, 397–414.

[26] Li, Z., Leduc, J., Nunez-Ramirez, J., Combescure, A., Marongiu, J.C., 2015. A non-intrusive partitioned approach to couple smoothed particle hydrodynamics and finite element methods for transient fluid-structure interaction problems with large interface motion. Computational Mechanics 55, 697–718.

[27] Liao, K., Hu, C., Sueyoshi, M., 2014. Numerical simulation of free surface flow impacting on an elastic plate, in: Proceedings of 29th Intl workshop on water wave and floating bodies, Osaka, Citeseer.

[28] Liao, K., Hu, C., Sueyoshi, M., 2015. Free surface flow impacting on an elastic structure: Experiment versus numerical simulation. Applied Ocean Research 50, 192–208.

[29] Lin, J., Naceur, H., Coutellier, D., Laksimi, A., 2015. Geometrically nonlinear analysis of two-dimensional structures using an improved smoothed particle hydrodynamics method. Engineering Computations 32, 779–805.

[30] Lind, S., Stansby, P., Rogers, B.D., 2016. Incompressible–compressible flows with a transient discontinuous interface using smoothed particle hydrodynamics (SPH). Journal of Computational Physics 309, 129–147.

[31] Lind, S., Xu, R., Stansby, P., Rogers, B., 2012. Incompressible smoothed particle hydrodynamics for free-surface flows: A generalised diffusion-based algorithm for stability and validations for impulsive flows and propagating

waves. Journal of Computational Physics 231, 1499–1523.
[32] Liu, M., Liu, G., 2010. Smoothed particle hydrodynamics (SPH): an overview and recent developments. Archives of Computational Methods in Engineering 17, 25–76.
[33] Lobovskỳ, L., Botia-Vera, E., Castellana, F., Mas-Soler, J., Souto-Iglesias, A., 2014. Experimental investigation of dynamic pressure loads during dam break. Journal of Fluids and Structures 48, 407–434.
[34] Marrone, S., Antuono, M., Colagrossi, A., Colicchio, G., Le Touzé, D., Graziani, G., 2011. Delta-SPH model for simulating violent impact flows. Computer Methods in Applied Mechanics and Engineering 200, 1526–1542.
[35] Marrone, S., Colagrossi, A., Chiron, L., De Leffe, M., Le Touzé, D., 2018. High-speed water impacts of flat plates in different ditching configuration through a Riemann-ALE SPH model. Journal of Hydrodynamics 30, 38–48.
[36] Marrone, S., Colagrossi, A., Di Mascio, A., Le Touzé, D., 2015. Prediction of energy losses in water impacts using incompressible and weakly compressible models. Journal of Fluids and Structures 54, 802–822.
[37] Marrone, S., Colagrossi, A., Park, J., Campana, E., 2017. Challenges on the numerical prediction of slamming loads on LNG tank insulation panels. Ocean Engineering 141, 512–530.
[38] Martínez-Ferrer, P.J., Qian, L., Ma, Z., Causon, D.M., Mingham, C.G., 2018. An efficient finite-volume method to study the interaction of two-phase fluid flows with elastic structures. Journal of Fluids and Structures 83, 54–71.
[39] Meringolo, D.D., Aristodemo, F., Veltri, P., 2015. SPH numerical modeling of wave–perforated breakwater interaction. Coastal Engineering 101, 48–68.
[40] Monaghan, J.J., 2005. Smoothed Particle Hydrodynamics. Reports on Progress in Physics 68, 1703–1759.
[41] Oger, G., Le Touzé, D., Guibert, D., De Leffe, M., Biddiscombe, J., Soumagne, J., Piccinali, J.G., 2016. On distributed memory MPI-based parallelization of SPH codes in massive HPC context. Computer Physics Communications 200, 1–14.
[42] Ren, J., Jiang, T., Lu, W., Li, G., 2016. An improved parallel SPH approach to solve 3D transient generalized Newtonian free surface flows. Computer Physics Communications 205, 87–105.
[43] Shadloo, M., Oger, G., Le Touzé, D., 2016. Smoothed particle hydrodynamics method for fluid flows, towards industrial applications: Motivations, current state, and challenges. Computers & Fluids 136, 11–34.
[44] Skillen, A., Lind, S., Stansby, P.K., Rogers, B.D., 2013. Incompressible smoothed particle hydrodynamics (SPH) with reduced temporal noise and generalised Fickian smoothing applied to body-water slam and efficient wave-body interaction. Computer Methods in Applied Mechanics and Engineering 265, 163–173.
[45] Sun, P.N., Colagrossi, A., Marrone, S., Antuono, M., Zhang, A.M., 2018a. Multi-resolution Delta-plus-SPH with tensile instability control: towards high reynolds number flows. Computer Physics Communications 224, 63–80.
[46] Sun, P.N., Colagrossi, A., Marrone, S., Antuono, M., Zhang, A.M., 2019. A

consistent approach to particle shifting in the δ-Plus-SPH model. Computer Methods in Applied Mechanics and Engineering 348, 912–934.

[47] Sun, P.N., Colagrossi, A., Marrone, S., Zhang, A.M., 2016. Detection of Lagrangian Coherent Structures in the SPH framework. Computer Methods in Applied Mechanics and Engineering 305, 849–868.

[48] Sun, P.N., Colagrossi, A., Marrone, S., Zhang, A.M., 2017. The δplus-SPH model: Simple procedures for a further improvement of the SPH scheme. Computer Methods in Applied Mechanics and Engineering 315, 25–49.

[49] Sun, P.N., Colagrossi, A., Zhang, A.M., 2018b. Numerical simulation of the self-propulsive motion of a fishlike swimming foil using the δ^+-SPH model. Theoretical and Applied Mechanics Letters 8, 115–125.

[50] Sun, P.N., Ming, F.R., Zhang, A.M., 2015. Numerical simulation of interactions between free surface and rigid body using a robust SPH method. Ocean Engineering 98, 32–49.

[51] Sun, P.N., Zhang, A.M., Marrone, S., Ming, F.R., 2018c. An accurate and efficient SPH modeling of the water entry of circular cylinders. Applied Ocean Research 72, 60–75.

[52] Turek, S., Hron, J., 2006. Proposal for numerical benchmarking of fluid-structure interaction between an elastic object and laminar incompressible flow, in: Fluid-structure interaction. Springer, pp. 371–385.

[53] Vacondio, R., Rogers, B., Stansby, P., Mignosa, P., 2016. Variable resolution for SPH in three dimensions: Towards optimal splitting and coalescing for dynamic adaptivity. Computer Methods in Applied Mechanics and Engineering 300, 442–460.

[54] Yang, X., Kong, S.C., 2019. Adaptive resolution for multiphase smoothed particle hydrodynamics. Computer Physics Communications .

[55] Ye, T., Pan, D., Huang, C., Liu, M., 2019. Smoothed particle hydrodynamics (SPH) for complex fluid flows: Recent developments in methodology and applications. Physics of Fluids 31, 011301.

[56] Zhang, A., Sun, P., Ming, F., 2015. An SPH modeling of bubble rising and coalescing in three dimensions. Computer Methods in Applied Mechanics and Engineering 294, 189–209.

[57] Zhang, A.M., Sun, P.N., Ming, F.R., Colagrossi, A., 2017. Smoothed particle hydrodynamics and its applications in fluid-structure interactions. Journal of Hydrodynamics, Ser. B 29, 187–216.

[58] Zhang, Y., Wan, D., 2018. MPS-FEM coupled method for sloshing flows in an elastic tank. Ocean Engineering 152, 416–427.

[59] Zhang, Z., Walayat, K., Chang, J., Liu, M., 2018. Meshfree modeling of a fluid-particle two-phase flow with an improved SPH method. International Journal for Numerical Methods in Engineering 116, 530–569.

[60] Zhang, Z.L., Feng, D.L., Ma, T., Liu, M.B., 2019. Predicting the damage on a target plate produced by hypervelocity impact using a decoupled finite particle method. Engineering Analysis with Boundary Elements 98, 110–125.